Computations of soliton impact onto a vertical wall: Comparing incompressible and compressible assumption with experimental validation

Marc Batlle Martin, Grégory Pinon, Julien Reveillon, Olivier Kimmoun

Coastal Engineering

Computations of soliton impact onto a vertical wall: Comparing incompressible and compressible assumption with experimental validation☆

Marc Batlle Martin [a], Grégory Pinon [a,*], Julien Reveillon [b], Olivier Kimmoun [c]

[a] Laboratoire Ondes et Milieux Complexes, Normandie Univ, UNIHAVRE, CNRS, LOMC, 76600, Le Havre, France
[b] CORIA, Normandie Univ, UNIROUEN, CNRS, CORIA, 76000, Rouen, France
[c] IRPHE, Centrale Marseille, France

ARTICLE INFO

Keywords:
Impact
Compressible
Incompressible
Impulse
OpenFOAM

ABSTRACT

This paper present numerical computations of solitary wave impact on a vertical wall. Different wave breaking cases were studied such as the high-aerated (air-pocket) or low-aerated (flip-through) in order to test the software ability to accurately reproduce the generated wall pressure loads. The numerical toolbox OpenFOAM was used here under the incompressible and compressible assumptions, together with 2D and 3D configurations. First, an idealised test case was used to validate the numerical convergence on an analytical value of the pressure impulse. Pressure impulse convergence was always numerically obtained but the pressure levels never converged under the incompressible assumption. Switching to the compressible assumption, pressure impulse and pressure time series converged both on the idealised test case and on the experimental configuration used. A large variety of spatial and temporal pressure variations were highlighted in this study that enable some physical interpretation of the impact mechanism.

1. Introduction

Coastal and offshore structures are subjected to catastrophic consequences under extreme sea state conditions. On the one hand, these extreme events constrain the structural design for long return period loads. Though less violent, winter storms also exert large pressure peaks mainly related to breaking waves. Liquid tanks subjected to oscillatory displacements such as the Liquefied Natural Gas (LNG) carriers are also confronted to the so-called sloshing problem. In this later case, the moving liquid can lead to wave breaking conditions producing similar extreme loads on the inner-shell of the tank. The understanding of the fluid solid impact problem has been largely studied with special focus on the highly transient pressure fields. When it comes to vertical breakwaters the guidelines developed by Goda (2010) are frequently used to compute the wave loads for non-breaking, broken and breaking waves (the latter with the Takahashi extension).

One of the first documentation on wave loading dates from 1840 by Stevenson (2011), where spring dynamometers and visual observation was employed on site at Dunbar, a UK harbour. Nothing really happened until 1937, when stepped wave gauges and piezo-electric transducers were used by de Rouville et al. (1938) in the port of Dieppe, France. Large scale impact pressures were recorded and highlighted the very localised and transient nature of these dynamic waves impacts. Afterwards, these results where employed to calibrate empirical model (e.g. Bagnold 1939). These studies already featured the wide pressure range between similar incoming waves. Investigations on smaller scale wave flumes using high-speed video techniques allowed to better understand the relation between the free surface shape and the pressure distributions, see Hattori et al. (1994) or Oumeraci et al. (1993) to cite two of the most relevant ones. Furthermore, the entrapment of air was observed as an important phenomenon during these impacts. More recent studies have been carried out on large scale facilities by Bullock et al. (2007), Cuomo et al. (2010) or Hofland et al. (2011). Four different breaking types, as; slightly-breaking, low-aeration, high-aeration and broken, were differentiated by Bullock et al. (2007). Particle Image Velocimetries (PIV) techniques were also used during small scale trials by

☆ This document is the results of the research project funded by the Agence Nationale de la Recherche, through the program Investissements d'avenir - LabEx EMC3 via the project PERCUSS.
* Corresponding author.
E-mail address: gregory.pinon@univ-lehavre.fr (G. Pinon).

https://doi.org/10.1016/j.coastaleng.2020.103817
Received 10 July 2020; Received in revised form 1 November 2020; Accepted 17 November 2020

Kimmoun et al. (2009) or Jensen (2018) among others. Or, the studies of Lugni, Miozzi, Brocchini and Faltinsen (2010b); Lugni, Brocchini and Faltinsen (2010a) who investigated the dynamics and kinematics of the compressibility effects for the sloshing problem in a depressurised tank.

This impact problem has also been studied by Cooker and Peregrine (1990), who proposed an analytical model based on the impulse theory highlighting the pressure impulse as a key parameter. As High Performance Computation becomes more and more affordable, this problem has also been investigated numerically using different techniques, such as Smooth Particle Hydrodynamic Techniques (SPH), e.g. by Guilcher et al. (2010), Oger et al. (2010) or Lind et al. (2015). The Finite Volume Method (FVM) using a Volume of Fluid (VoF) approach has also demonstrated good capabilities. There are different referenced works using this method. For instance, Hu et al. (2017) used an incompressible two-phase solver from the OpenFOAM library to reproduce the four breaking types and compared them with the experimental results from Mai et al. (2015). More recently, a compressible solver from the OpenFOAM library has been used by Liu et al. (2019) and compared with the aforementioned large scale experiments Bullock et al. (2007).

The present work somehow lies in the continuation of the aforementioned studies and uses an incompressible and a compressible solver from the OpenFOAM package to further investigate the local pressures on these kind of events. The scope of this paper concerns very large and sudden impact pressures caused by breaking waves on vertical solid structures. More precisely, the aim is to reproduce numerically the peak pressure magnitudes for such impulsive behaviours. The wave breaking types described as air-pocket or high-aerated and flip-through are employed as they are reported Hattori et al. (1994); Bullock et al. (2007) to produce the higher pressure magnitudes. But beforehand, a convergence study of both incompressible and a compressible approaches is performed regarding pressure and impulse values to prove confidence and robustness of the methodology. This paper is organised as follows: Section 2 briefly describes the numerical method in OpenFOAM. Then, an incompressible approach is first used in Section 3 on an idealised impact configuration to test convergence, followed by realistic wave impacts. Section 4 is dedicated to similar configurations but with the compressible approach. Comparisons with experimental results of realistic wave impact from Kimmoun et al. (2009) are also presented and discussed. The last Section 5 presents a 3D computation of the high-aerated impact before final conclusions and perspectives.

2. Numerical model

The present section describes the numerical model core equations. An algebraic interface advection scheme is examined and the addition of compressibility effects is introduced in the last subsection.

2.1. Governing equations

The problem will be treated as an homogeneous two-phase fluid: immiscible with no slip between phases. This allows us to use a single momentum equation and velocity field to model both phases. The solver employs a finite volume spatial discretisation and Volume Of Fluid (VOF) to track the free surface. The flow variables are cell centred, but their face interpolated values are also used in the solution procedure.

Firstly, the continuity equation is presented in eq. (1). This states the mass rate of change in a fluid element, plus the net mass flow of the fluid element, such as:

$$\frac{\partial \rho}{\partial t} + \nabla\cdot(\rho\mathbf{u}) = 0 \tag{1}$$

When the fluid is assumed as incompressible, this last equation turns into:

$$\nabla\cdot\mathbf{u} = 0 \tag{2}$$

where ρ is the fluid density and **u** the velocity vector in a cell.

Secondly, the single momentum equation for the homogeneous mixture model is:

$$\frac{\partial \rho\mathbf{u}}{\partial t} + \nabla\cdot(\rho\mathbf{u}\mathbf{u}) = -\nabla p + \rho\mathbf{g} + \nabla\cdot\left[2\mu\left(\nabla\mathbf{u} + (\nabla\mathbf{u})^T\right)\right] + \sigma\kappa\nabla\alpha \tag{3}$$

where p stands for the pressure, **g** the gravitational acceleration vector, μ the dynamic viscosity, σ is the surface tension coefficient and $\kappa = \nabla\cdot(\nabla\alpha/|\nabla\alpha|)$ the mean curvature of the interface. Finally, α is the liquid volume fraction used for the Volume Of Fluid (VOF).

The model employs a modified pressure p_d rather than p, introducing a density gradient (near the interface) and their relation is given by:

$$p_d = p - \rho\mathbf{x}\cdot\mathbf{g}, \nabla p_d = \nabla p - \rho\mathbf{g} - \mathbf{x}\cdot\mathbf{g}\nabla\rho \tag{4}$$

The transient flow problem is solved using the PIMPLE algorithm, which is a combination between the PISO (Issa, 1986) (Pressure Implicit with Splitting of Operator) and SIMPLE (Patankar and Spalding, 1972) (Semi-Implicit Method for Pressure-Linked Equations).

2.2. The treatment of interfaces

To capture the nature of the interface between phases denoted by $\mathscr{A}$ and $\mathscr{B}$ in the physical domain $\mathscr{D}$ (satisfying $\mathscr{A}\cup\mathscr{B} = \mathscr{D}$), an indicator field is introduced:

$$\mathbb{I}(\mathbf{x},t) = \begin{cases} 1 & for\ \mathbf{x}\in\mathscr{A}(t) \\ 0 & for\ \mathbf{x}\in\mathscr{B}(t) \end{cases}. \tag{5}$$

This function has a singular nature and the integration of this quantity over a computation cell Ω_i yields to the volume fraction α of fluid $\mathscr{A}$ defined as the following:

$$\alpha_A(\mathbf{x}_i,t) = \frac{1}{|\Omega_i|}\int_{\Omega_i}\mathbb{I}(\mathbf{x},t)dV. \tag{6}$$

The transported volume fraction α_A (here water) ensures by definition the algebraic relation $\alpha_A + \alpha_B = 1$ in each computational cell. Then, the density field can be evaluated such as:

$$\rho = \rho_A\alpha_A + \rho_B\alpha_B. \tag{7}$$

Finally, the liquid volume fraction continuity equation is derived from the general continuity eq. (1) by introducing eq. (7). The following phase continuity equation is obtained in terms of volume fraction and reads:

$$\frac{\partial \alpha_k\rho_k}{\partial t} + \nabla\cdot(\alpha_k\rho_k\mathbf{u}) = 0, k = \{A,B\}. \tag{8}$$

This equation shows a diffusive behaviour of the interface, although the physical interface should be negligibly thick macroscopically. To tackle this problem, different treatment of the advective term of eq. (8) exist, such as geometric (see Roenby et al. 2016) or algebraic, the latter being described in the following.

The algebraic method modifies the advection term itself. This approach uses low order schemes far from the interface region and high order schemes near the interface. To define the vicinity of the interface, a delimiter called MULES (Multidimensional Universal Limiter with Explicit Solution) will be used. Defining the cell faces as f, the cell face area vector as $\mathbf{S}_f$ and the velocity vector on a cell face as $\mathbf{u}_f$; the volume flux on a computational cell face will the be $\varphi_f = \mathbf{u}_f\cdot\mathbf{S}_f$. Once this is said, the advection term near the interface takes the following form:

$$\nabla\cdot(\alpha\mathbf{u}) = \frac{1}{|\Omega_i|}\sum_{f\in\partial\Omega_i}\varphi_f\alpha_f + \varphi_{rf}\alpha_f(1-\alpha)_f, \tag{9}$$

where a summation of all fluxes over all faces f is performed on each computation cell surface $\partial\Omega_i$. The second term in the summation is

known as the compressive flux φ_{rf} defined by:

$$\varphi_{rf} = min\left(C_\alpha \frac{|\varphi_f|}{|\mathbf{S}_f|}, max\left[\frac{|\varphi_f|}{|\mathbf{S}_f|}\right]\right)(\mathbf{n}_f \cdot \mathbf{S}_f). \tag{10}$$

here, the constant C_α is a user-defined value, which serves as a parameter to restrict the interface smearing. Vector $\mathbf{n}_f = \frac{(\nabla\alpha)_f}{|(\nabla\alpha)_f|}$ is the face centred interface normal. This term $\mathbf{n}_f$ artificially acts on cells close to the interface only (with low fractions of air or water), compressing them to obtain the sharpest interface possible constrained by the cell size. For further details on this interface capturing method, see Deshpande et al. (2012) or Damián (2013).

2.3. Differences between the compressible and incompressible solver

Fluids compressibility is governed by equations of state (EOS). These EOS are not unique for each fluid but for a fluid undergoing a specific process. They define the density variation according to other physical field variables. In the present work, both phases are trated as compressible undergoing an adiabatic process using a "stiffened" EOS. This EOS reads:

$$p + p^* = (\gamma - 1)e\rho, \tag{11}$$

where γ is the specific heats ratio and e is the internal energy per unit mass. Last equation (11) presents a modification of the standard EOS for perfect gas $p = (\gamma - 1)\rho e$ first presented by Cole (1948) in his study of *Underwater explosions* by adding the constant p^* value. Using the Euler equation, a relation between the phase speed of sound C and this constant p^* can be extracted as the following:

$$C = \sqrt{\frac{\gamma \cdot p + p^*}{\rho}}. \tag{12}$$

This constant will take different values: of the order of 1 *bar* for air, or much larger than 1 *bar* for water as a matter of example.

The resolution process follows a similar procedure as the one presented under the incompressible assumption. One of the major difference stands in the fact that the pressure resulting from the momentum equation will be employed for the EOS to calculate the new density field. This will be introduced into a modified liquid volume fraction transport equation that reads:

$$\frac{\partial \alpha}{\partial t} + \nabla \cdot (\alpha \mathbf{u}) = -\frac{\alpha}{\rho}\left(\frac{\partial \rho}{\partial t} + \mathbf{u}\nabla\rho\right), \tag{13}$$

Finally changing the liquid volume fraction field α. The assumption of barotropic fluids (eq. (12)) allows the possibility of not solving the energy equation, increasing the computational speed.

3. Solitary wave impact onto a vertical wall - 2D incompressible formulation

In this section, the incompressible assumption is tested for impulsive impact cases. First, an idealised test case is presented arising the strengths and weaknesses of this assumption on such events. Then, a realistic breaking wave is computed and analysed for a 2D configuration wave channel.

3.1. Idealised wave impact on a vertical wall

When a fluid strikes a body at rest, very large forces are generated over a very short period of time and the instantaneous Newton's Second Law is of little use in this situation. Instead, it looks more convenient to use the pressure impulse I theory (Lagrange 1811), defined as:

$$I(\mathbf{x}) = \int_{t_b}^{t_a} p(\mathbf{x}, t)dt, \tag{14}$$

where t_b and t_a are the instants before and after the impact respectively (see Fig. 1).

In order to study this problem, a simple configuration is defined, where the change in velocity is supposed to take place over such a short time that the nonlinear convective terms in the equation of motion are negligible compared with the time derivative. Also the viscosity and surface tension effects can be neglected. The impact speed has to be much lower than the speed of sound in the liquid, making the incompressible assumption realistic. For a sake of simplicity, the gravity is set to zero in this theoretical case. Under the aforementioned circumstances, the procedure is: first to integrate over the impact interval and, second to make use of the pressure impulse definition (eq. (14)) over the momentum equation (eq. (3)). Then, the pressure impulse satisfies the following Laplace's equation:

$$\nabla^2 I = 0. \tag{15}$$

The 2D idealised impact test case of Cooker and Peregrine (1995) is used in the present work. The test-case consists of an idealised square wave impinging on a vertical wall in a two-dimensional boundary problem, so that an analytic solution of the previous Laplace equation (15) could be found. Fig. 2a describes the rectangular fluid domain with free surfaces at the upper and right-hand edges. Fluid is in contact with the bottom and left-hand rigid walls. An initial constant value of velocity U_0 normal to the wall will be set in all the fluid domain. The analytical solution of this problem is found using separation of variables and Fourier analysis Cooker and Peregrine (1995), such as:

$$I(x,z) = \rho H \sum_{n=1}^{\inf} a_n sin(\lambda_n z / H) \frac{sinh[\lambda_n (b-x)/H]}{cosh(\lambda_n b/H)}, \tag{16}$$

with $-H \le z \le 0$ and $0 \le x \le b$, where $\lambda_n = (n - 0.5)\pi$ and the constants a_n are:

$$a_n = 2U_0 \frac{cos(\lambda_n) - 1}{\lambda_n^2}. \tag{17}$$

This configuration is modelled with two different phases (water and air) as depicted in Fig. 2a with $H = 0.05m$ and $L = 0.1m$. Here the liquid phase is already in contact with the left wall from the start of the simulation; this makes the solution independent from the interface jump. The boundary conditions are set to solid wall for left and bottom boundaries, and as open boundaries for top and right edges. The separation between the open boundaries and the water region is chosen largely to avoid any influence on the solution. An uniform orthogonal

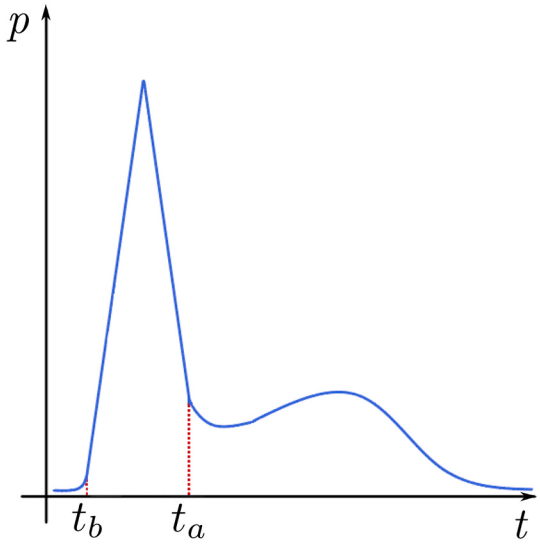

Fig. 1. Typical pressure record during wave impact.

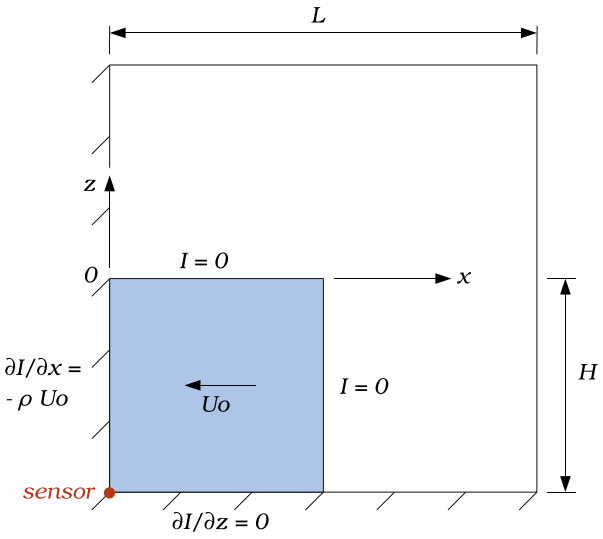

(a) Schematic representation of an idealised wave impinging on a vertical wall.

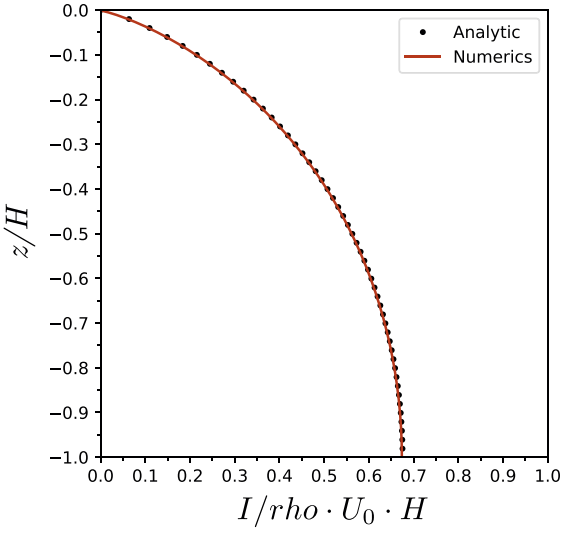

(b) Wall pressure impulse distribution compared with the Cooker and Peregrine (1995) analytic solution, $dh/H = 2 \times 10^{-3}$ and $maxCo = 0.01$.

Fig. 2. Impact of an idealised wave on a vertical wall.

mesh is equally distributed in all the domain, with mesh sizes ranging from $2.5 \times 10^{-4} \leq dx/H = dz/H \leq 4 \times 10^{-3}$. An initial velocity $U_0 = 1\ m/s$ is set in the water region. Only the first few time-steps are run in order to capture the impact phenomenon, and the wall pressure distribution is recorded in all the cell face centres of the left boundary at each time step.

The pressure impulse (eq. (14)) is highly dependant on the definition of t_b and t_a. In the present study, the impulse area is approximated by an isosceles triangle and the rise time as half of the triangle base (see Fig. 1). In the present simulations, the maximum peak pressure is reached after the first computed time step and thus, the rise time is equal to the initial time step. Using these definitions, the computed impulse distribution is shown in Fig. 2b and compared with its analytical counterpart, all divided by a characteristic linear momentum of the liquid block. A perfect agreement is obtained in terms of magnitude and wall distribution between the computed and the analytic solution proposed by Cooker and Peregrine (1995) for the mesh discretisation $dh/\ H = 2 \times 10^{-3}$ and a variable time discretisation constrained by a maximum Courant number $C_0 = U \cdot \Delta t / \Delta h = 0.01$.

Fig. 3 displays maps of the dimensionless pressure impulse (Fig. 3a) and the velocity field (Fig. 3b) at the impact instant for the water phase only ($\alpha < 0.5$). The pressure gradient (Fig. 3a) decelerates the liquid from an initial velocity field U_0 to a new one (Fig. 3b), generating a strong liquid jet. This last feature was also described analytically by Cooker and Peregrine as a velocity singularity when $x \to 0$ at the upper

Table 1
Simulation results of an idealised wave impact for different spatial discretisations. Results extracted from the numerical pressure sensor presented in Fig. 2a

dh/H	$t_{imp}[s]$	p [bar]	$I/(\rho \cdot U_0 \cdot H)$
4×10^{-3}	1×10^{-6}	336	0.672042
2×10^{-3}	4.54×10^{-7}	741	0.673706
1×10^{-3}	2.04×10^{-7}	1652	0.674537
5×10^{-4}	9.34×10^{-8}	3611	0.674954
2.5×10^{-4}	4.31×10^{-8}	7831	0.675167

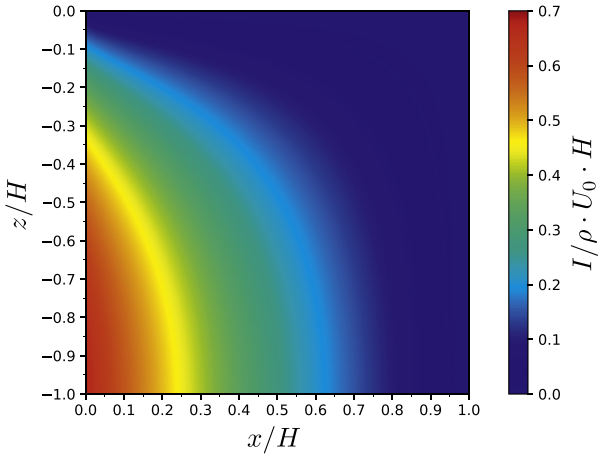

(a) Adimensional pressure impulse

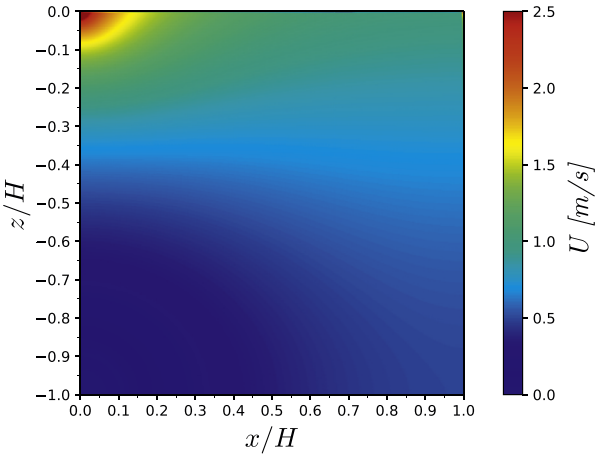

(b) Velocity magnitude

Fig. 3. Adimensional impulse and velocity magnitude in the liquid region using a cell size.$dh/H = 2 \times 10^{-3}$

water surface.

In order to check convergence, different spatial (Table 1) and temporal (Table 2) discretisations have been tested. Table 1 presents the results while refining the mesh, where dh refers to the cell length, t_{imp} the first time step or the rise time, p the peak pressure and I the impulse. The successive mesh refinements result in an asymptotic behaviour of the velocities and, when the maximum Courant Number C_o is imposed, this results in a time-step Δt drop as observed in Table 1. The small domain and the very few time steps employed for these computations allow affordable computational costs, even when using such fine discretisations as $dh = 0.0125mm$ ($dh/H = 2.5 \times 10^{-4}$). In these simulations, the maximum Courant number was fixed at $C_0 = 0.01$ and, thus, when reducing the cell size the time step decreased proportionally. A reasonably good stability and convergence of the impulse towards the analytic value of $0.675314(\rho U_0 H)$ is presented. From Fig. 4, one can observe that the peak pressure keeps increasing, by approximately a factor of two as the cell length decreases by a fixed factor of 0.5.

Table 2 presents the results while modifying the time step by limiting the maximum Courant number and using $dh = 0.1mm$ as cell length. The pressure peak also diverges while refining the time discretisation. Finally, Fig. 5 presents the results of both tables in terms of adimensional impulse and initial time step. The analytic solution is also represented using a dashed black line. This graph depicts the fact that only lowering the time step will not improve the pressure impulse towards the analytic solution. Although, a combination of both spatial and temporal refinement present a tendency towards the solution proposed by Cooker and Peregrine. It is also important to remark the fact that fixing the time-step and refining the cell length stabilises the pressure peak, although, this will not be realistic as it would strongly depend on the selected time-step. To conclude, this analysis arises the stability of the solver dealing with an impulsive situation by means of the impulse convergence. However the pressure fields are presented as unreliable under the incompressible assumption for this kind of computations.

3.2. Description of the solitary wave impact test case

The next section focuses into a realistic wave impact phenomenon using experimental data from Kimmoun et al. (2009) under laboratory conditions. First the experimental setup and results will be briefly introduced to contextualise the numerical results.

The experiments were performed in a 17 m long, 0.65 m width and 1.2 m height wave flume, with a 1/15 slope starting at 3.95 m away from the wave generator which will produce the wave overturning, see Fig. 6a. The waves were generated using a flap type wave maker. A flexible plate with an embedded base and simple support was located 14.5 m away from the wave generator, see Fig. 6b. Multiple pressure gauges were added on the plate to record pressure series with an acquisition frequency of $16kHz$. One of the objectives during the experiments was the study of the plate deflection and in order to allow this, two backlashes of 2 mm were left between the plate and the lateral walls in both sides. Furthermore, this separation allows the air and water to flow through during the impacts. This fact had a noticeable effect during the impact process and will be further analysed.

Two breaking types are evaluated, using the definitions of Bullock et al. (2007): the air-pocket or high-areated configuration (see Fig. 7a) or the flip-through (see Fig. 8a). To perform this study, a solitary wave following the Boussinesq theory is employed facilitating the analysis of a singular impact event, without any reflected or incoming wave train. The experimental wave parameters for the air-pocket case defined in the flat bottom part, were set such as $H = 0.0864m$ for the amplitude and a water depth of $h = 0.7185m$, resulting in a shallow water based steepness of $H/h = 0.1202$. Using 1% of the maximum wave height to determine an equivalent wave length L, a value of $L = 15m$ is obtained together with the celerity in shallow water $c = 2.8m/s$ and the equivalent period $T = 5.349s$. Secondly, for the flip-through case, the amplitude is $H = 0.0627m$, the water depth is $h = 0.7185m$ and a steepness of $H/h = 0.0872$ is obtained. These two plunging waves have in common an impulsive behaviour when interacting with a wall while their overturning process.

Table 2
Simulation results of an idealised wave impact for different temporal discretisations.

$maxC_o$	$t_{imp}[s]$	p [bar]	$I/(\rho \cdot U_0 \cdot H)$
0.1	5×10^{-6}	67	0.673783
0.05	2.5×10^{-6}	134	0.673742
0.01	4.54×10^{-7}	741	0.673706
0.005	2.22×10^{-7}	1 515	0.673702
0.001	4.45×10^{-9}	75, 588	0.673697

Figs. 7 and 8 represent the velocity field instants before the impact extracted from Particle Image Velocimetry (PIV) and the plate pressure distribution for the two breaking at the highest peak pressure instant. In the PIV images (left picture), the red horizontal lines on the plate indicate the location of the pressure sensors. In the air-pocket case Fig. 7, it is observable, on the velocity field of the left picture, how the highest velocities are located on the jet with values around $2m/s$ pointing towards the plate. This case entraps high volumes of air between the liquid and the wall. The flip-through configuration presents velocities of approximately 1.6 m/s pointing towards the plate in a small localised area. In this situation, a small volume of air is entrapped.

Regarding the pressure distribution, each colour represent different width coordinates (Figs. 7b and 8b) on the plate and the black line is the average value at each height. In the air-pocket, the highest peak pressure is only recorded by one sensor at $Z = 0.073$ m on the central section. The pressure sensors inside the air cavity, $Z = 0.053$ m and $Z = 0.043$ m, have significant differences between sections caused by the air escape on the side of the wall. Besides this, a general 2D assumption seems acceptable regarding the pressure sensor in the impact point, $Z = 0.063$ m, which captured very similar magnitudes in two different sections. The flip-through impact maintains similar pressure ranges between different transverse sections of the plate. This is normal because the time for the water to escape is much longer than for air. Much higher peak pressure values are recorded and seem to be more localised on the Z direction. This will be further developed and analysed in the following sections.

3.3. Numerical setup

Now a general view of the numerical setup to model the realistic wave breaking impacts is presented. The geometry is maintained as in the experiments. A static wave generator Higuera et al. (2013) is employed following the Boussinesq theory, which is based on shallow water depths assumptions. This causes minor differences on the wave propagation and a slight calibration is needed to reproduce the experimental liquid interface instants before the impact. The static wave generation boundary imposes the alpha and velocities fields, on the boundary cell faces, according to the adopted wave theory. Furthermore, an active wave absorption procedure corrects each time step the reflected waves (for further detail see Higuera et al., 2013). The right and the bottom boundary conditions are set as solid walls with a no slip condition for velocity. The top side is modelled by an open boundary with a total pressure condition where air and water can freely flow out and only air can flow in. Finally, the lateral sides are set to indicate a two-dimensional problem.

The employed mesh has two major zones in the vertical direction: above and below the red line in Fig. 9. The upper part has a geometric gradation having bigger cells close to top boundary and, the lower region mostly filled with liquid, the cell height is fixed in order to accurately capture the interface. Regarding the horizontal direction, a successive refinement by a factor of 0.5 define 4 regions, see Fig. 9,

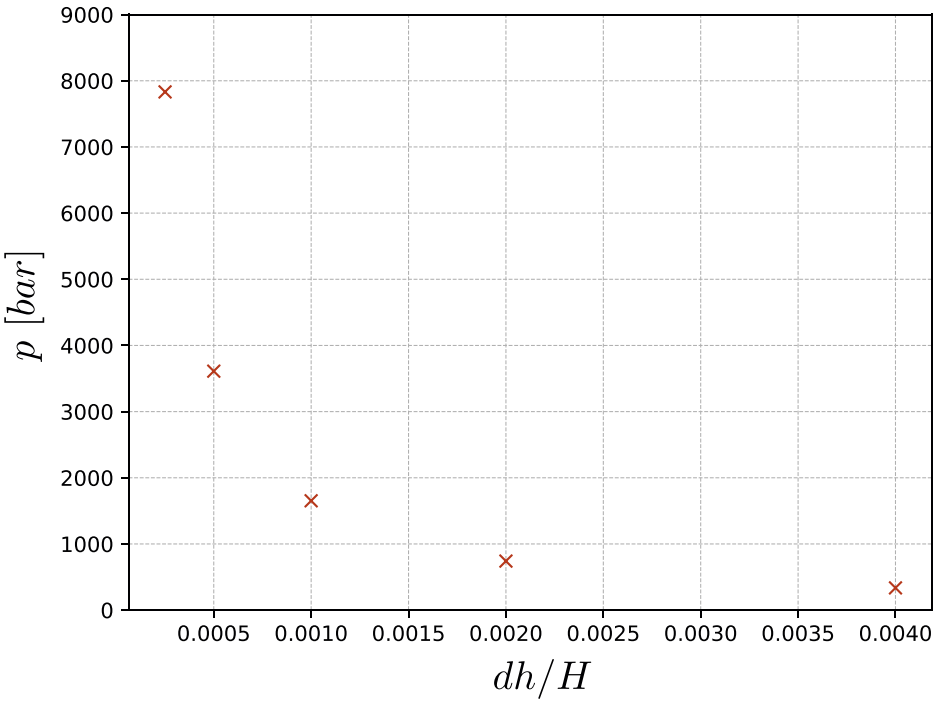

Fig. 4. Maximum peak pressure at the wall for different spatial discretisations.

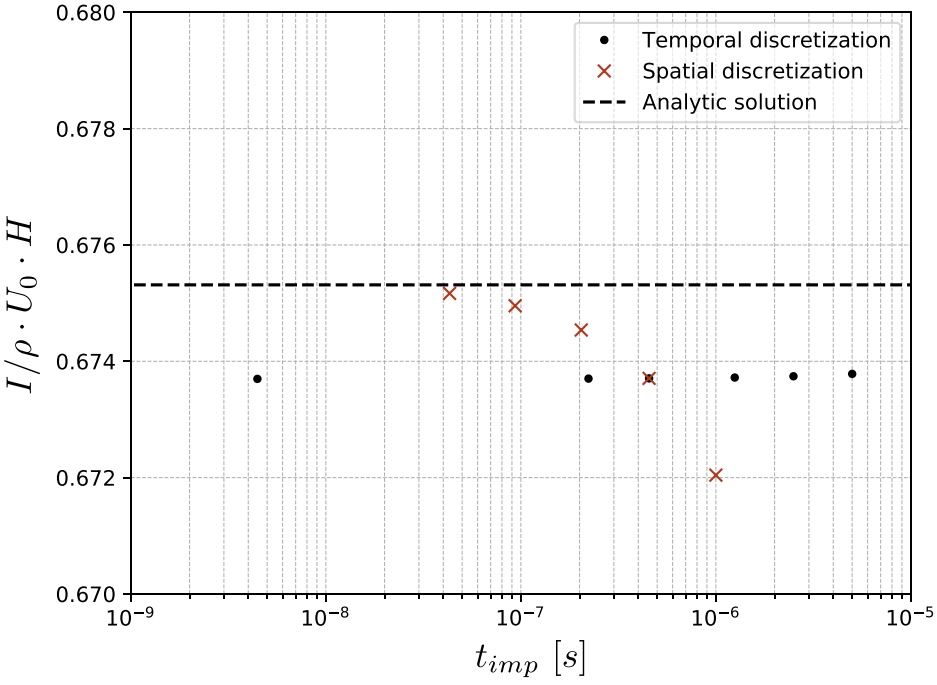

Fig. 5. Spatial and temporal discretisation comparison regarding the dimensionless pressure impulse.

where the coarser is close to the inlet and the finest keeping a cell aspect ratio of 1 on the impact area. Over the slope the cells are parallel to the plane except on the impact region where they will keep a 90deg angle with the vertical plate. Here, triangular cells are thus needed to fit the mesh with sloped plane. This bottom boundary cells will reduce the resolution of the run-up wave kinematics but allow orthogonal cells on the overturning region and close to the impact boundary, which have shown to produce less erratic impact results in terms of pressure on the impact wall cell faces. The finest mesh employed in this 2D configuration had 4.6 millions cells and a cell length at the impact region of $dh = 0.5\,mm$. A simulation of 9s is performed, as in the laboratory experiments with a maximum Courant number of 0.5. It takes 23 h with 28 cores of an Intel Broadwell (2.4 GHz) in CRIANN (Centre Régional Informatique et d'Applications Numériques de Normandie). This calculation time is disproportionately divided between approximately 5 h to compute the first 8s as the wave propagates and 18 h for the overturning and impact. As it will be examined later, the instants before the impact produce high speed air flows that drop the time-steps drastically, increasing then the computational time.

For these simulations, a kinematic viscosity of $1 \times 10^{-6} m^2/s$ was

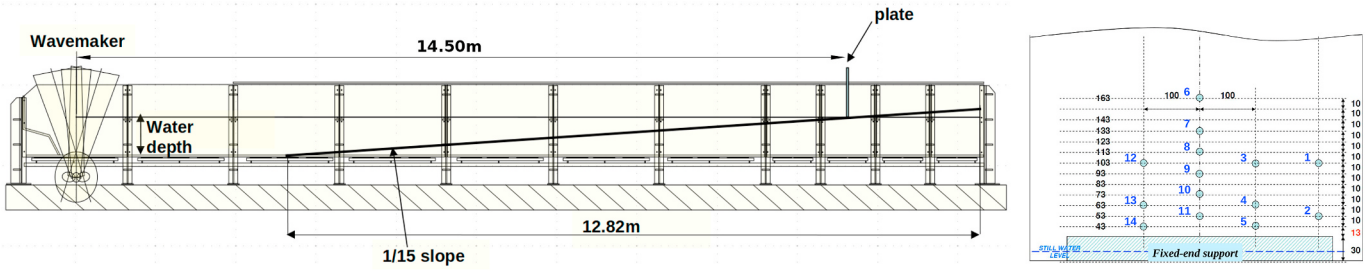

(a) Wave channel sketch X-Z

(b) Impact plate Y-Z. Units in cm

Fig. 6. Experimental wave channel sketch.

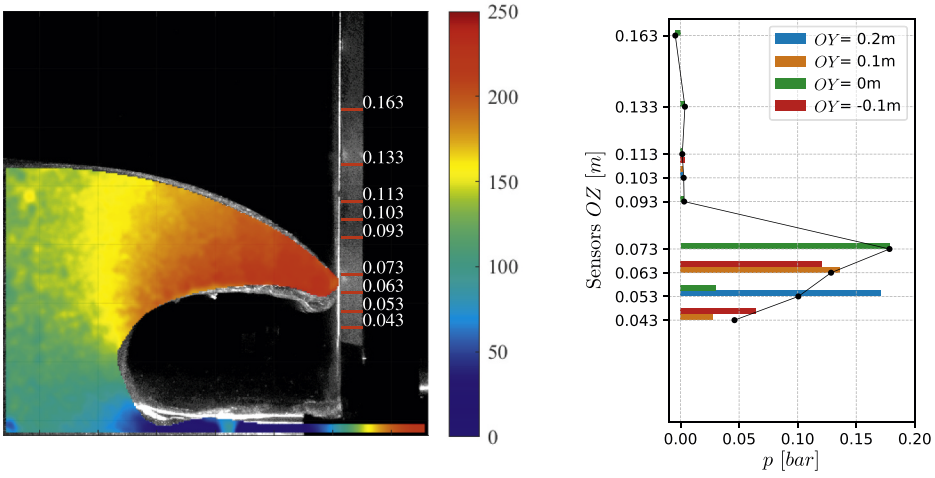

(a) Particle Image Velocimetry of an air-pocket impact. Colour range in cm/s

(b) Pressure distribution on the impact plate. The colors correspond to different pressure gauges that are at the same elevations but for different cross positions. The black line is an average of the pressure data.

Fig. 7. Experimental high-areated or air-pocket impact.

used for water and $1.48 \times 10^{-5} m^2/s$ for air. The density was kept as $1.2\ kg/m^3$ for air and $1000\ kg/m^3$ for water. Although the problem faced here is an inertial driven flow, the surface tension was kept with a constant value of 0.07. From Sumer et al. (2010), the Reynolds number for a solitary wave over a slopped beach (applicable in the up-rush phase) can be defined as: $Re_u = a(U_{0m})/\nu$, where ν is the kinematic viscosity, a is half of the stroke of the water particle displacement in the free-stream region and U_{0m} is the maximum free-stream velocity. For the present study, the maximum wave amplitude is $H = 0.0864\ m$ and the water depth out from the slope $h = 0.7185\ m$, thus the maximum Reynolds number at the slope during the run-up phase is $Re = 103000$ which is within the laminar flow ($Re < 2 \times 10^5$) defined by Sumer et al. (2010). It is also presented in the work of Higuera et al. (2018), on the supplementary materials, how the SST $k - \omega$ does not have a great impact on the dynamics and kinematics before the impact compared to the laminar model. Thus, a laminar model has been adopted in this work for the sake of simplicity. The boundary layer is roughly approximated using the Blasius boundary layer solution Schlichting and Gersten (1979). For the two wave conditions employed in this work, it takes values around $2.3mm$ on the horizontal bottom region and decreases throughout the swash zone. This boundary layer is out of the scope of the present work and even the finest mesh is not enough to resolve it properly. This is expected to contribute on the discrepancies against the experiments.

3.4. Air-pocket or high-areated impact

This section focuses on the wave breaking air-pocket impact under the incompressible assumption for both phases in a two dimensions configuration. Two major numerical challenges are faced in this kind of impact: on the one hand, the complex geometry of a narrow jet of liquid with high curvatures of the interface, and, on the other hand, the existence of high pressures peak within small time intervals.

To begin with, a qualitative study of the impact process is present in Fig. 10 with three snapshots of the dynamics and kinematics of the phenomenon. The images time referenced is shifted so that the highest pressure peak is reached at $t = 0\,s$. The first image shows the fields before the impact at the pressure rise time. The second one is at the impact instant and the third during the splash phenomenon. The pressure fields are presented for both air and water using the same scale, although, the pressure range is different for each instant to be representative. On the contrary, the velocity fields have different scales for both phases and keep the same range for the three instants. The interface is presented as a black solid line referenced by the contour of the liquid volume fraction field $\alpha = 0.5$.

First from Fig. 10a, one can observe how the incoming wave momentum is being absorbed by the air entrapped inside the cavity before the collision occurs. Here, the confinement process exacerbates the pressure gradient in front of the water spike increasing the air velocity

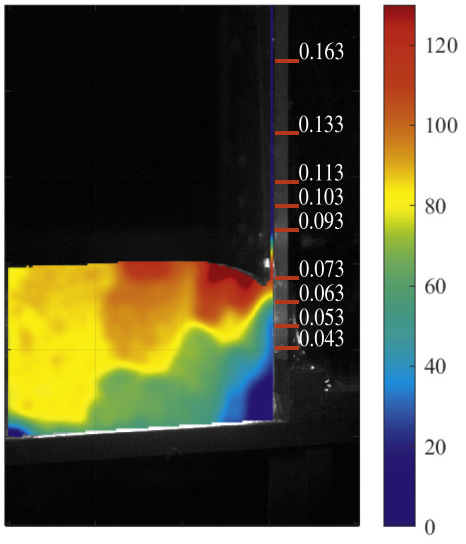

(a) Particle Image Velocimetry of a flip-through impact. Colour range in cm/s

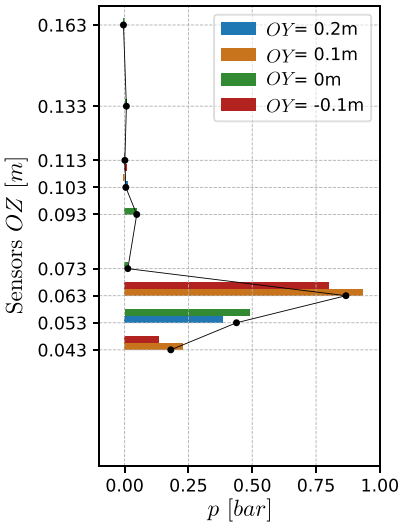

(b) Pressure distribution on the impact plate. The colors correspond to different pressure gauges that are at the same elevations but for different cross positions. The black line is an average of the pressure data.

Fig. 8. Experimental low-areated or flip-through impact.

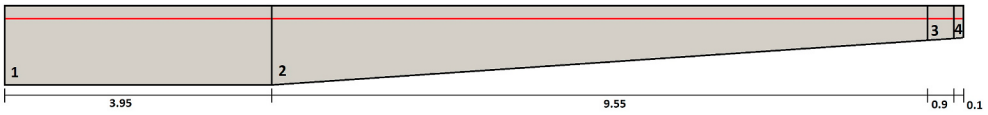

Fig. 9. Mesh sketch.

that flows out from the cavity. This fast air flow drags upwards a fraction of water, leading to a transformation of the water spike into a vertical narrow jet front. Comparing the water region before the impact with the PIV experimental images, presented in Fig. 7a, acceptable similarities in terms of velocities magnitude are presented. At the impact moment, Fig. 10b, the whole cavity has a constant pressure value due to the incompressible assumption and the most pronounced pressure gradient is shown. This fact is not observed in any representative experiments (see Bullock et al., 2007 or Kimmoun et al., 2009) where the air cavity region has a lower pressure magnitude on the wall than the impinging jet area. The highest peak pressure is reached as well as a fast deceleration of the water jet. At this point, the air can no longer escape freely from the cavity and pushes upwards the water front to expand the cavity volume. This is observed in Fig. 11a where the highest pressure records are localised on the splash jet directed upwards. As the cavity volume increases the inner pressure falls.

Now a mesh sensitivity analysis is presented regarding the capability of the solver and the interface method to model such a phenomenon. Four meshes with a factor of 0.5 refinements are studied and presented in terms of: free surface profile before the impact, pressure distribution on the wall at the impact moment and maximum pressure serie on the wall. First, Fig. 11a represents the free surface instants before the impact. The grid convergence is partially achieved regarding the free surface as it is part of a whole process of: propagation, run-up and overturning. During this process, a poorly resolved boundary layer and the interface energy dissipation leads to slightly different wave shapes. The free-surface is extracted at different instants for each mesh to be comparable, as the celerity will also vary slightly.

Next, the wall pressure records are studied on Figs. 11b and c an further detailed in Table 3 The pressure distribution on the wall at the impact moment confirms the fact that the whole cavity keep a constant pressure at the impact moment, as shown in Fig. 10b.

The selected series in Fig. 11c belong to the cell face on the wall where the maximum peak pressure is reached within the impact area. The series are shifted in time so that the impact moment occurs at $t = 0\ s$ and each serie corresponds to different elevations of the wall depending on the mesh configuration impact point. These pressure series present abrupt rises of pressure of the order of $0.02 - 0.1\ bar$ less than $1\ ms$ before the main peak pressure arrives. Then, the impact event is presented as the main peak pressure with high slopes on the rise time and lower on the fall. After the jet impact, a pressure valley is presented just before the collapse of the cavity which will lead to the splash phenomenon as the second pressure rebound. This second pressure rise is due to a strong jet of air trying to escape from the cavity through the front part of the overturning wave and pushing upwards with high velocity the liquid phase (see Fig. 10c). Depending on the violence of this jet, a smooth rebound $dh = 2\ mm$ is observable which turns to be more steep as the mesh is being refined to $dh = 0.5\ mm$. With respect to the maximum pressure value, once again the peak pressure keeps increasing when the cell size is being reduced. On the other hand, the rise time decreases while refining the mesh. These behaviours are similar to what was observed in Sec.3.1.

In this realistic wave impact, the definition of the impulse is calculated as an integral under the pressure serie (see Fig. 1). Now, the time before the impact t_b is the instant where the pressure slope will remain approximately constant until the peak pressure. Consequently, this

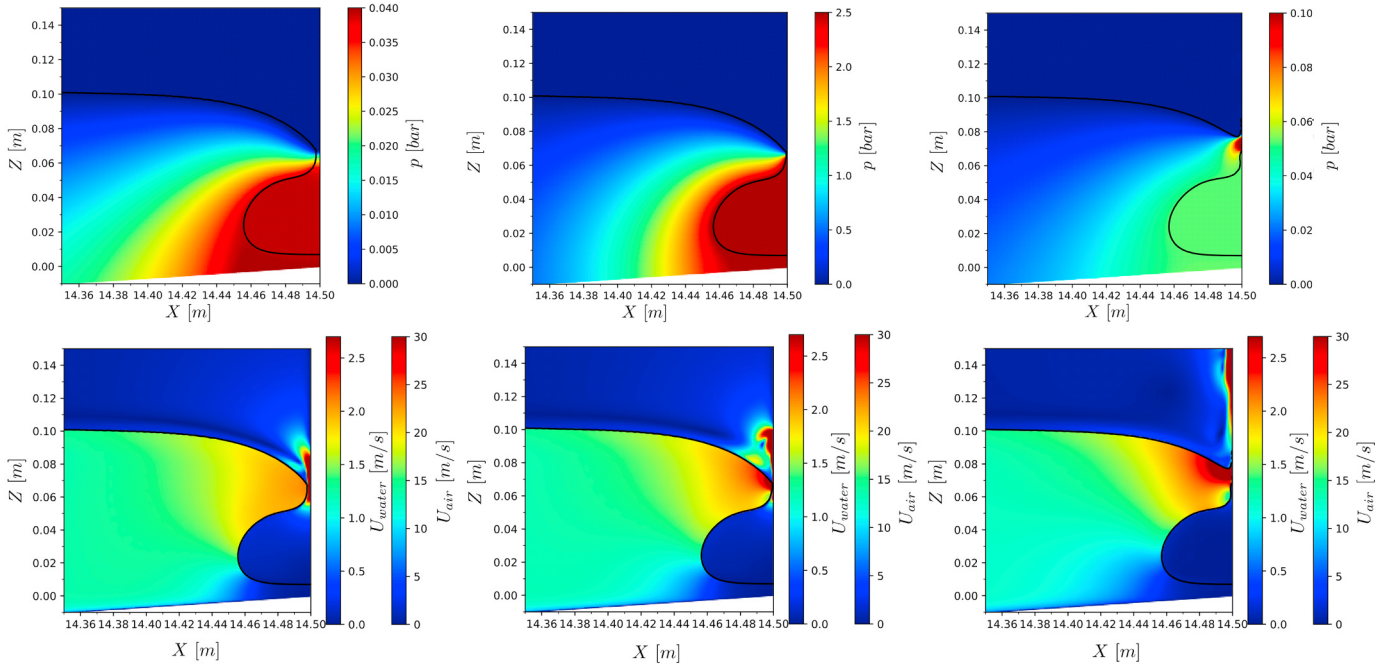

(a) Before the impact $t = -0.00066\ s$ (b) Impact instant $t = 0\ s$ (c) Splash after the impact $t = 0.002\ s$

Fig. 10. Two phase air-pocket impact under the incompressibility assumption using $dh = 0.5\ mm$. Solid line corresponds to the interface. Top: pressure evolution during the impact with a different pressure range at the different instants. Bottom: velocity magnitude for air and water.

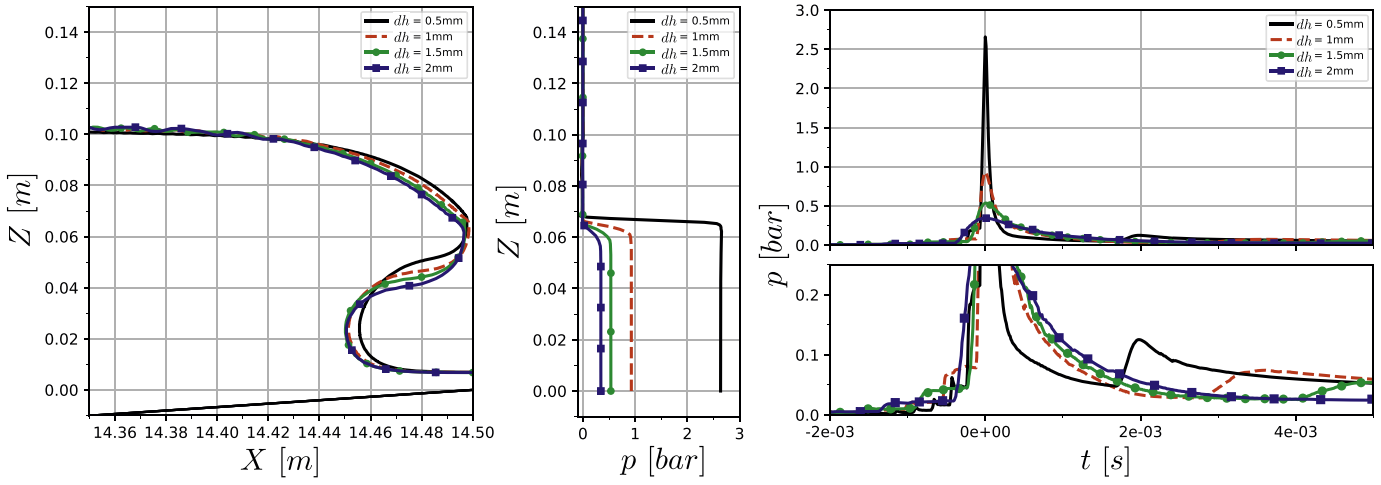

(a) Free surface (b) Pressure distribution on the wall (c) Maximum pressure serie on the wall

Fig. 11. Mesh convergence analysis
**dh*: refers to the impact region cell length.

Table 3
Pressure and impulse impact study for different spatial discretizations.

$dh[mm]$	2	1.5	1	0.5
$pMax[bar]$	0.344	0.537	0.93	2.656
$\Delta t[s]$	4×10^{-4}	2.3×10^{-4}	1.2×10^{-4}	7×10^{-5}
$I\ [N\cdot s/m^2]$	35.18	35.72	35.97	36.2

defines the rise time expressed in Table 3 as Δt. The time after the impact t_a is defined here as the same point for all different meshes as $t = 0.0014\ s$ where the function slope is approximately 45° with the horizontal. After these definitions, the obtained results are presented in Table 3 where a good convergence on the pressure impulse is achieved, similarly to what was obtained on the idealised wave configuration. With such results, it turns out that the incompressible assumption in a 2D configuration may lead to erroneous pressure peaks when studying such impulsive events.

4. Solitary wave impact onto a vertical wall - 2D compressible formulation

Following the impossibility to obtain converged peak pressure values under the incompressible assumption, a new approach using a

compressible solver is evaluated in this section. First the idealised wave case is employed to study the strengths and weaknesses of this assumption on such events. Next, two realistic breaking waves are modelled and analysed focusing on the compressibility role on a 2D configuration wave channel. A mesh sensitivity analysis is regarded for the air-pocket impact, followed by a comparison with the experimental data in terms of pressure records on the wall for both high and low aerated impacts.

4.1. Idealised wave impact on a vertical wall

The idealised wave case presented in Sec. 3.1 is now employed here with the same configuration and boundaries as shown in Fig. 2a. The main difference now is the compressibility of phases with a time-dependant density. To the best of the author's knowledge, similar numerical studies comparing incompressible and compressible fluids during impulsive events have been studied using Lagrangian codes, e.g. Marrone et al. (2015) As presented in Sec. 2.3 both phases follow now barotropic state equations. The system temperature is 20 $^{\circ}C$ and the initial pressure is set to atmospheric $p_0 = 1\ bar$. The air properties are, $\rho_{air} = 1.2\ kg/m^3$ for initial density, a constant specific heat ratio of $\gamma_{air} = 1.4$ and $C_{air} = 343\ m/s$ as a speed of sound. For water, $\rho_{water} = 1000\ kg/m^3$, a constant specific heat ratio of $\gamma_{water} = 7$ and $C_{water} = 1500\ m/s$. An initial velocity U_0 pointing perpendicularly to the left boundary is imposed on the water region. An implicit second-order pure Crank-Nicolson scheme is employed for the time derivative in all the simulations. These computations will run using a fixed time-step related to the Courant number and the speed of sound, following the relation $C \cdot \Delta t < n \cdot \Delta x$ presented by Braeunig et al. (2009), where C is the speed of sound, Δt the time-step, n a user defined value which is set as 0.1 initially and Δx the cell length.

In this situation, the water volume impinges the wall with an abrupt pressure rise and a reduction of water density in the vicinity of the wall (Fig. 12). This produces a pressure wave which propagates through the water domain similarly as a sound wave. As the pressure wave moves away from the impacted wall, it trails a small region of the liquid that starts a fast compression-expansion behaviour. A pressure gradient will form from the free surface top edge advancing towards the bottom boundary as the pressure wave moves, allowing gradually the entrapped water to gain velocity upwards. In Fig. 12a it is observable the pressure wave in the water region at $t = 2.5 \times 10^{-5}\ s$ advancing symmetrically to the bottom boundary with an approximate speed of 1100 m/s. Fig. 12b presents the velocity field magnitude at the same instant. Here the region unaffected by the pressure wave still has initial inertial velocity of 1 m/s pointing towards the left wall. The compressed region has almost a null velocity, and, at the free boundary top edge the water jet is gaining velocity upwards (top left of Fig. 12b).

Fig. 13a depict different gauge pressure ($p = p_{abs} - p_0$) series from different locations of the left wall. During the very first impact times ($0 < t < 2 \times 10^{-6}\ s$), very high pressure oscillations are recorded on the different locations, simultaneously for all the impact region. As the pressure wave moves forward it decelerates the incoming fluid and liberates gradually the entrapped liquid behind. The liquid region close to the bottom wall will remain under pressure until the pressure wave front is far enough. The situation presented here, as the water domain is square shaped the pressure drop at $z/H = -1$ occurs approximately at $t = 4.5 \times 10^{-5}\ s$ when the pressure wave reaches the right liquid boundary. At this instant an expansion front moves vertically, from the bottom boundary towards the free surface, dropping the pressure into subatmospheric values. The second graph, Fig. 13b, presents the pressure impact results at $z/H = -1$ for different spatial discretisations and linked time-steps (see Table 4). This study depicts a good convergence of the results in terms of the peak pressure, which is close to the acoustic pressure solution of $p = \rho \cdot C \cdot u = 15\ bar$. On the other hand, the rise time t_{imp} decreases as the mesh is refined with the same factor. The oscillations frequency increases as the cell length decreases, as well as the compression-expansion trailing region gets smaller. Finally, Fig. 13c, presents the pressure impact results at $z/H = -1$ for different temporal discretisations using $dh/H = 4 \times 10^{-3}$ mesh. It is observable a direct relation between the peak pressure and the simulation time-step (see Table 5). When the time-step is reduced the peak pressure slightly increases within an error $E = (p_{acoustic} - p_{numeric})/p_{acoustic}$ lower than 10%. Time-step values in the order of $n \cdot (\Delta x / C)$ present good results with an error of 2.6% if selecting the constant $n = 0.1$, as in Braeunig et al. (2009). Although, a value of $n = 0.0375$ presents in this case a perfect agreement with the acoustic pressure prediction of 15 bar (see Table .5). The simulation using $\Delta t = 5 \times 10^{-10}\ s$ takes 920 steps before the peak pressure and, thus, the numerical diffusion should be taken into account.

Table 4 presents a good convergence in terms of peak pressure while refining the spatial discretisation, where, dh refers to the cell length, Δt the time step, t_{imp} the rise time and p the peak pressure. On the other hand, Table 5 presents the peak pressure results while refining the temporal discretisation. This section presented the robustness of the solver to evaluate fluid impulsive pressures when taking into account the compressibility effects.

4.2. Air-pocket or high-areated impact

This section focuses on the air-pocket impact under the compressibility assumption for both phases, following the barotropic EOS eq. (11), in a two dimensions configuration. To begin with, a qualitative study of the impact process is presented in Fig. 14. The reference time is

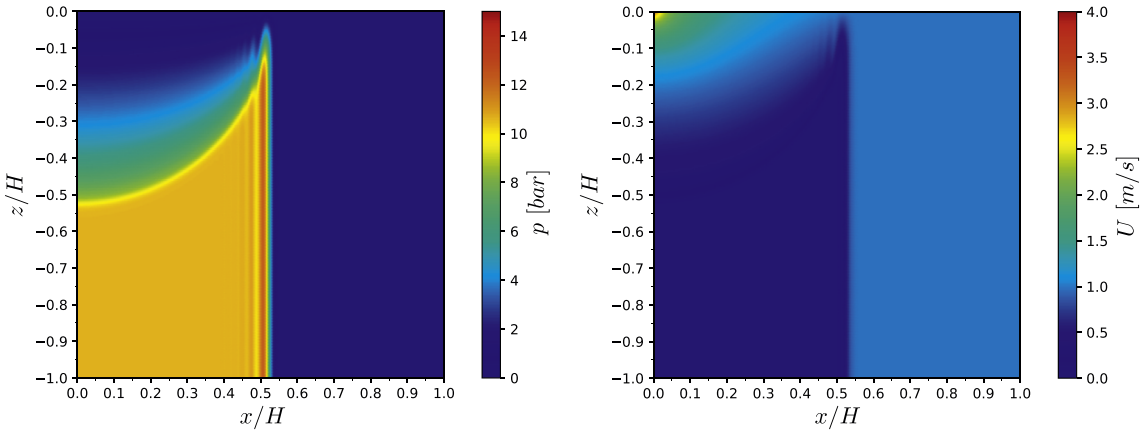

(a) Pressure (b) Velocity magnitude

Fig. 12. Pressure and velocity magnitude on the liquid region using a cell size $dh/H = 2 \times 10^{-3}$ at.$t = 2.5 \times 10^{-5}\ s$

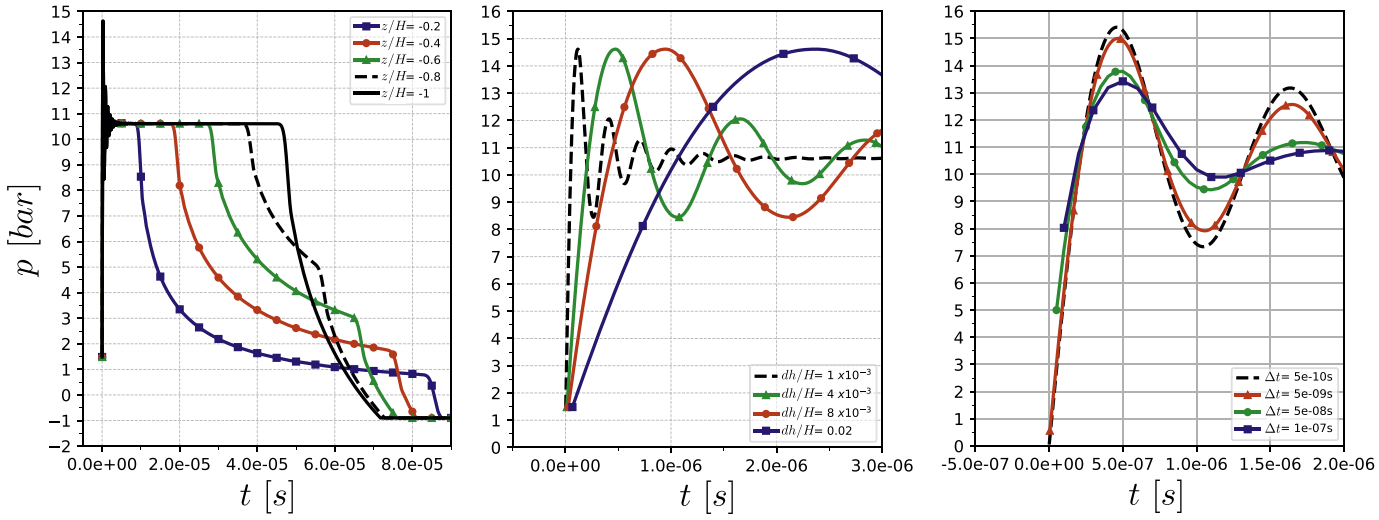

(a) Different elevations ($dh/H = 2 \times 10^{-3}$) (b) Mesh convergence ($z/H = -1$) (c) Time-step convergence ($z/H = -1$)

Fig. 13. Pressure series on the impact wall.

Table 4
Spatial discretisation convergence.

dh/H	$\Delta t[s]$	$t_{imp}[s]$	p [bar]
0.02	6.66×10^{-8}	2.4×10^{-6}	14.613
8×10^{-3}	2.66×10^{-8}	9.6×10^{-7}	14.614
4×10^{-3}	1.33×10^{-8}	4.8×10^{-7}	14.614
1×10^{-3}	3.33×10^{-9}	1.16×10^{-7}	14.612

Table 5
Temporal discretisation convergence.

$\Delta t[s]$	n	$t_{imp}[s]$	p [bar]
1×10^{-7}	0.75	5×10^{-7}	13.42
5×10^{-8}	0.375	5×10^{-7}	13.78
5×10^{-9}	0.0375	4.7×10^{-7}	15
5×10^{-10}	0.00375	4.6×10^{-7}	15.41

shifted so that the highest pressure is reached at $t = 0\,s$. The first Fig. 14a represents an instant before the impact. Here the air cavity is being rapidly enclosed and the pressure starts increasing. The air is forced to leave the cavity through the space between the wall and the water spike front. The air outflow speed increases as the water spike approaches the wall and it will stop as soon as the water meets the wall. Once this happens, the deceleration of the water spike is balanced by a fast pressure rise to stop the moving liquid. There is only one stagnation point where the velocity is equal to zero, on each side of this point the liquid escapes up and down. In Fig. 14b the highest peak pressure is located in the water impact area and the cavity, still pressurised, will reach lower values. This differs from what was presented under the incompressible assumption, see Fig. 10b, where both the air and the water region had the same pressure value at the impact moment. Finally, the splash phenomenon occurs when two water jets go upwards and downwards from the impact area avoiding the obstacle, Fig. 14c. This last phenomenon are characterised by dynamic pressures in the order of $p = \rho u^2$.

Further understanding of this process can be extracted from the pressure fields recorded in every time step on the wall cell centres. Fig. 15a presents a typical pressure record on the water impact area undergoing a 2D high aerated impact ($z = 0.067\,m$). In this region, the fast deceleration and the higher density will lead to the highest pressure values in this kind of events. Three main phenomenons are presented here; first the peak pressure related to the high density phase impact ($0 < t < 0.01\,s$). Secondly and until $t < 0.2\,s$, a process of pressure oscillations due to an anisotropic contraction and expansion behaviour of the air cavity; this behaviour has already been reported experimentally in Oumeraci et al. (1993), Hattori et al. (1994) or Bullock et al. (2007). This process ($t > 0.2\,s$) could be related to a spring effect of the compressibility of the gas pocket. The shape and area of the cavity will have a great effect on the magnitude and damping of these oscillations. Moreover, this air cushioning effect evokes the necessity of a two phase solver and has been studied before from a different perspective using Lagrangian methods, e.g. Marrone et al. (2016). Finally, a tended rebound of quasi-hydrostatic pressure is presented during the run-up phase. This has not been completely computed as it is out from the impulsive scope of this work and involves a turbulent behaviour.

Now four numerical pressure sensors near the impact point are analysed in Fig. 15b. The black continuous line is a zoom ($-0.01\,s < t < 0.01\,s$) of the impact instants already presented in Fig. 15a. The red sensor located inside the air cavity is the first to be pressurised with a gradually growth as the air cavity is being enclosed. It will have a cushioning effect reducing the whole event violence. The black sensor simultaneously climbs on pressure until a sudden jump presents the highest peak pressure. This happens when the water spike meets the wall. The location of the peak pressure is located on the water spike impact area, however, it will move relatively between the red and the blue sensors depending on the water spike shape and disposition. After the impact, the pressure drops and rebounds as the air cavity is being gradually pressurised due to the incoming wave. Before impact ($-0.0025\,s < t < -0.001\,s$), the atmospheric pressure remains constant on the blue sensor $Z = 0.073\,m$ until a subatmospheric pressure happens just before the water meets the wall. This subatmospheric pressure has also been reported experimentally by Hattori et al. (1994) or Kimmoun et al. (2010) and is produced by the high speed air flowing out before the entrapment. Next the steepest pressure rise occurs when the liquid first meets the wall and keeps increasing levelling the air cavity

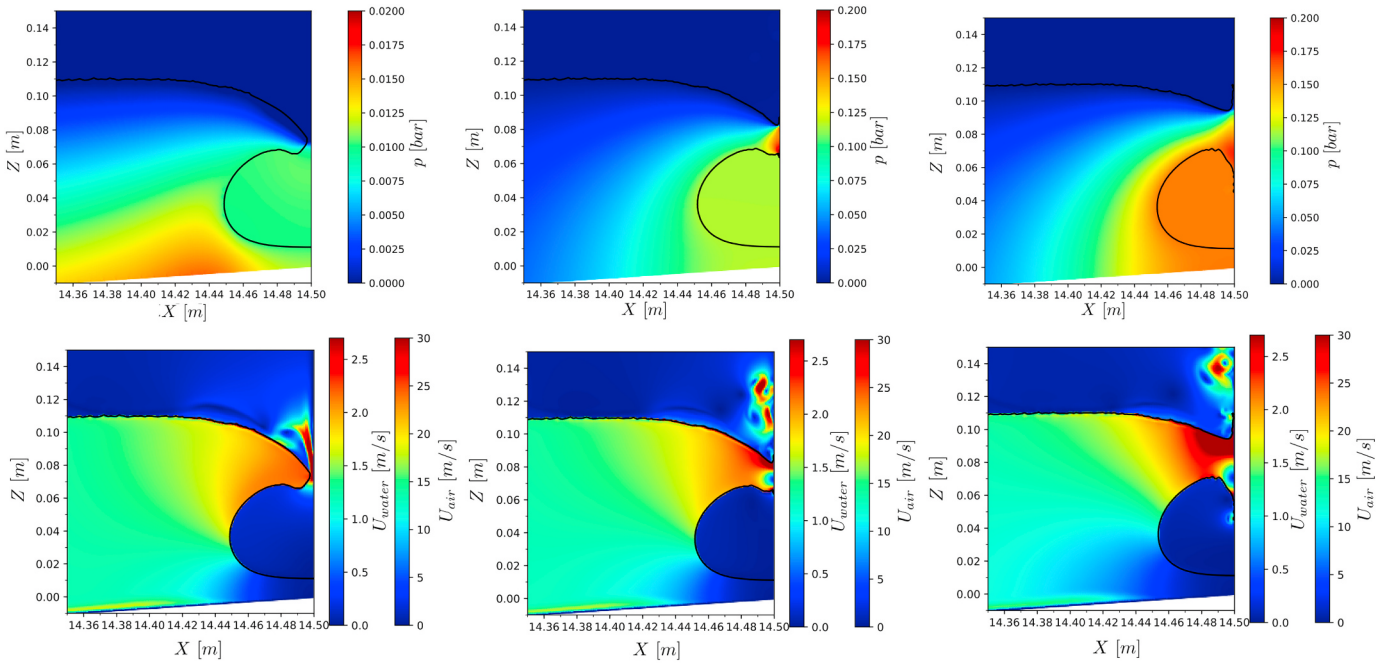

(a) Before the impact $t = -0.00243\ s$ (b) Impact instant $t = 0\ s$ (c) Splash after the impact $t = 0.00257\ s$

Fig. 14. Two phase air-pocket impact under the compressibility assumption using $dh = 0.5\ mm$. Solid line corresponds to the interface. Top: pressure evolution during the impact with different pressure ranges at the different instants. Bottom: velocity magnitude for air and water.

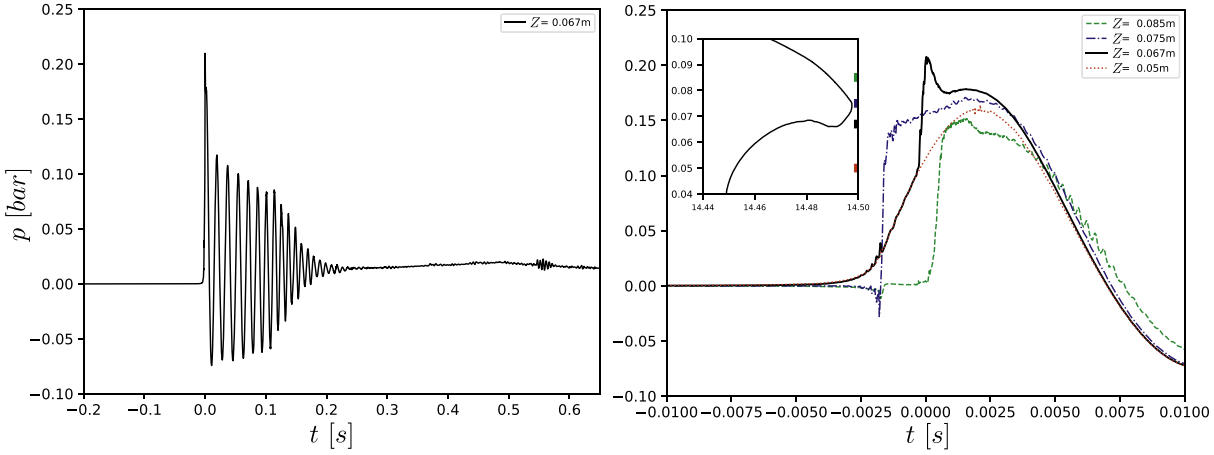

(a) Maximum pressure serie (b) Different elevation pressure series

Fig. 15. Pressure records during a 2D air-pocket or high aerated impact.

pressurisation. To end with, a sensor (green dashed-line) above the impact area is also affected by the air jet depressurisation. It will not increase in pressure until the splash phenomenon starts and then it will further be pressurised by the cavity compression.

Now a mesh sensitivity analysis is carried out, in terms of free surface and pressure fields, with a spatial refinement factor of 0.5. These meshes are referenced by the characteristic cell length dh in the impact area (region 4 of Fig. 9). Fig. 16a compares the free surface profile before the impact. A partial convergence is achieved due to the interface diffusion and a poorly boundary layer resolution during the wave: propagation, run-up and over-turning. Therefore, the pressure record with the highest peak pressure, being highly sensitive to the water spike, is located at different elevations and instants. Fig. 16b presents this highest pressure signal recorded on the wall at $Z = 0.052\ m$ for the coarser mesh (blue dashed-dotted) and $Z = 0.067\ m$ for the finest (black line). This last configuration corresponds to the one presented on Fig. 15. The signals were shifted so that the highest pressure is reached at $t = 0\ s$. The most relevant feature is the stability of the peak pressure around 0.2 *bar* while refining the cells size, hence slightly modifying the water spike geometry. Besides this fact, the pressure rise before the impact has some differences between the finest and the coarser mesh. This may originate from the faster arrival of the peak pressure. To further develop this, as it was mentioned from Fig. 15b, the peak pressure may not occur at the very first liquid-solid contact but will depend on the incident angle and front shape of the water spike. The pressure rise due to compression of the air cavity, with a lower slope than the fluid impact, has two major differences between discretisations: on the one hand, a lower maximum value of the first compression related to smaller volume of air being entrapped by the coarser mesh $dh = 2mm$; and on the other hand, a sooner appearance of this compression linked to the fact that the

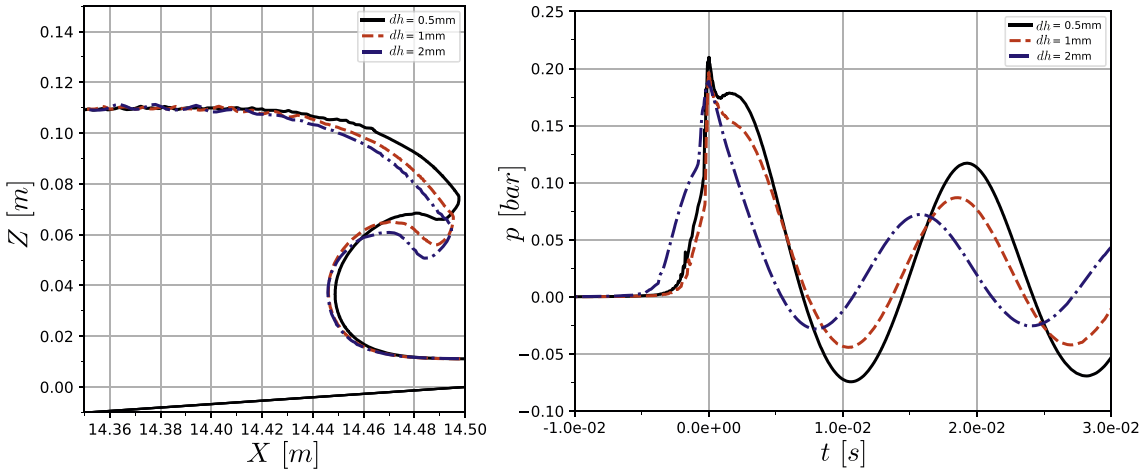

(a) Free surface (b) Maximum pressure serie on the wall

Fig. 16. Mesh convergence analysis. dh refers to the characteristic cell length in the impact region denominated as 4 in Fig. 9.

presented pressure record is closer to the air cavity with the coarser mesh.

The convergence of the results towards a stable solution while improving the mesh resolution gives confidence to compare now the numeric results with the experimental data. The finest mesh $dh = 0.5\,mm$ is employed in the forthcoming comparisons. To achieve the better experimental-numerical comparison, it is necessary to reproduce the kinematics and fluid geometry moments before the impact. The chosen experimental wave parameters for this case were a soliton amplitude of $0.0864\,m$ and a water depth of $0.7185\,m$. However, as mentioned before, the wave maker during the experiments was a flap and here a piston type is employed. This will arise slight differences during the propagation and, thus, a parametrization study regarding the water depth and amplitude was carried out to obtain the most comparable profile before impact. The numerical amplitude employed for this case is $0.0844\,m$ and a water depth of $0.7165\,m$, which produces the interface profile shown in Fig. 17a. Differences can be seen in terms of surface elevation in the order of *mm* and lower depth regarding the quasi static fluid under the air cavity. The air cavity has a smaller area when compared with the experiments and the numerical water spike is narrower. Furthermore, very low amplitude oscillations are observable at the top part of the wave due to some parasitic currents on the low density phase near the interface. This phenomenon has been already and largely reported in the literature, linked to the surface tension term on an initial stage (see Francois et al. 2006; Hysing 2006 or Larsen et al. 2018) and extended to inertial flows due to an imbalance on the pressure and the density gradient terms near the interface (see Wemmenhove et al. 2015 or Vukčević, Jasak and Š. Malenica 2016). Here these wiggles remain small enough not to affect the inertial driven flow during the next few seconds. Although this discrepancies with the experiments, a fairly good agreement is achieved and allows a fair comparison in terms of loads on the wall.

Fig. 17b compares pressure distributions at the instant when the maximum pressure peak is reached numerically and the averaged maximum pressure distribution from the experiments, as it was presented in Fig. 7. The relative low number of pressure sensors during the experiments and the variability between the different transverse sections enables only a approximate comparison. But both numerically and experimentally, the peak pressure is reached in the vicinity of the water impact region. However, the numerical distribution reaches the highest

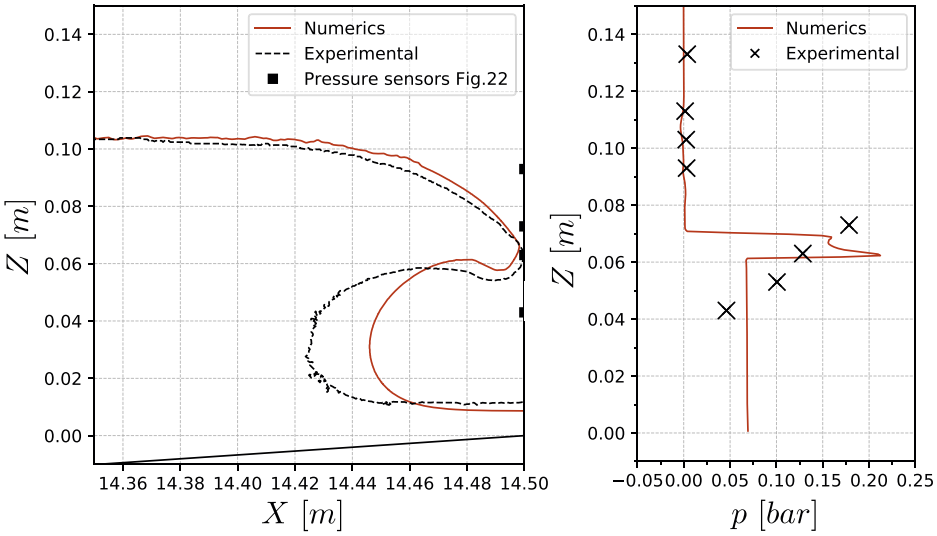

(a) Free surface (b) Pressure distribution on the wall at $t = 0\,s$

Fig. 17. Free surface and pressure distribution comparison at the impact moment.

peak pressure slightly beneath the initial contact point. Regarding the experiments the maximal pressure is reached above the initial impact point. Inside the air cavity, at $Z = 0.053\ m$, the average pressure records extracted from the different sensors (at different transverse location) have very different values $\Delta p = 0.14\ bar$ and the presented averaged value may not be completely representative. On the contrary, the sensor at $Z = 0.043\ m$ has a more reliable value in the experiments and presents a overestimation of the numerical results. This fact is expected from the 2D configuration which does not allow the air from the cavity to flow out using the backlash in the transverse OY direction. Above the impact area, the pressure values remain as atmospheric pressure both numerically and experimentally speaking.

Fig. 18 depicts a closer comparison to four temporal pressure series with the experiments. As mentioned above, the temporal series are shifted so that the highest peak pressure is reached at $t = 0\ s$ experimentally and numerically. Slight time lag are observed due to the different geometries between the numerical and the experimental results. The behaviour inside the air cavity ($Z = 0.043m$) experiences a rise of pressure at the first instant. Experimental and numerical records are initiated following a similar trend, even though their evolution rapidly separate from each other. Sinusoidal like oscillations are produced numerically by compression and expansion of the air entrapped with an approximate initial frequency of 80 *Hz*. The simulation reaches a higher value of 0.14 *bar* during this first compression of the cavity and a subatmospheric minimum of 0.058 *bar* in the first expansion. This pressure oscillation phenomenon is not appreciable on the experiments after the first rebound. Here the compression of the cavity, with a lower pressure range of 0.08 *bar*, pushes the air to flow on the transverse direction reducing the pressurisation to normal atmospheric values. This is followed by a pressure plateau of 0.06 *bar* produced by a water jet going downward from the impact point. The expansion and contraction of the air cavity is completely damped after 0.3*s*. This phenomenon will affect all the pressure signals with in the influenced area during these interval.

A focus will now be made on the region where the water spike meets the wall: between $Z = 0.063\ m$ and $Z = 0.073\ m$. A detail of the impact interval is shown on the left part of Fig. 18. At $Z = 0.063\ m$, the highest numerical peak pressure of 0.21 *bar* is reached. The presented rise in pressure has two main origins: an initial rise produced by the air-cavity compression and a second, with higher values, by the water impact. Approximately 1 *ms* after the peak, the pressure drops and is followed by a second rebound when the air cavity if fully compressed (see bottom left graph of Fig. 18). Similarly, the experimental record presents a lower maximum pressure peak at 0.14 *bar* then followed by the air-cavity compression lead pressure rise. Next it follows a similar trend as the simulation, with a pressure fall and a second rebound simultaneously with the air cavity maximum compression. The peak pressure then seems to be a superposition of water spike momentum and the cavity pressurisation effects. Finally, the numerical results will not capture the experimental behaviour, where the possibility for the air to flow out will prevent the subatmospheric oscillations. At $Z = 0.073\ m$, the highest experimental peak pressure of 0.17 *bar* is reached (see top left graph of Fig. 18). Here the high slope on the pressure rise is originated initially only by the water impact. Numerically the peak pressure is underestimated due to a lower water impact region.

The pressure sensor above the water impact ($Z = 0.093m$) represents the splash phenomenon and the run-up. Here both numerics and experiments experience at the same time a pressure rise when the splash phenomenon occurs. Small subatmospheric pressure drops are captured experimentally and numerically at different instants before this pressure rise. The air-cavity compression and expansion will also affect this higher part of the wall arising a clear physical phenomenon differentiation between the experiments and the simulation.

Finally, a coloured map of the evolution of pressure field on the wall is presented in Fig. 19. The cavity compression before the water jet meets the wall is presented in lighter blue below $Z < 0.065\ m$. Less than 1 *ms* before the maximum peak pressure, the water meets the wall and a sudden pressure rise is observed at the impact area, coloured as the orange arrowhead. After that, the peak pressure in dark red is located beneath this point having a downward direction as the water jet influence starts expanding. At $t = 3\ ms$ the cavity reaches the maximal compression and starts the expansion process. From this map, the air-cavity compression-expansion oscillating phenomenon can clearly be observed.

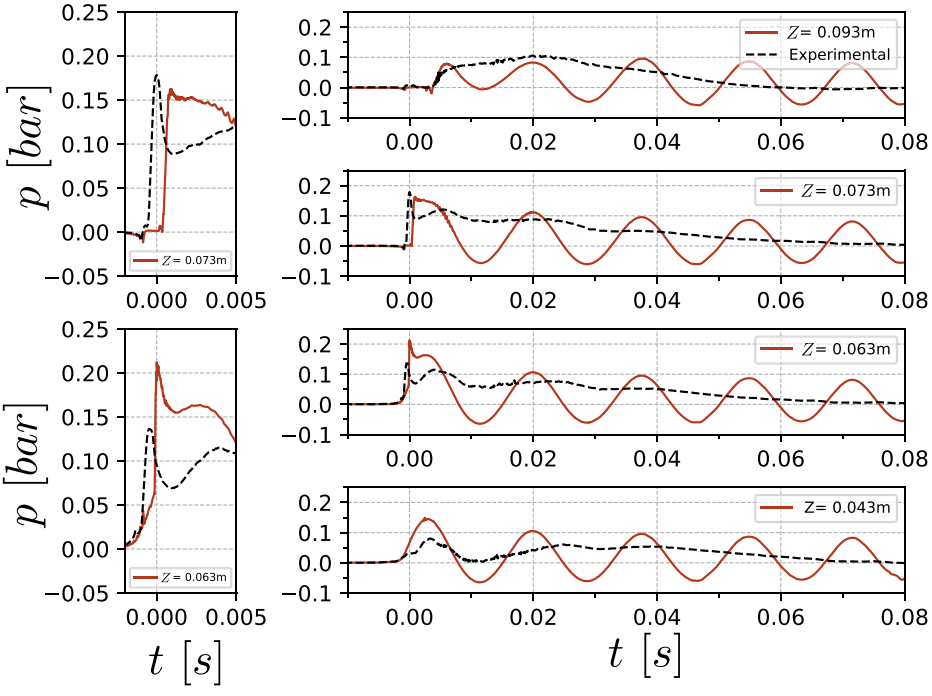

Fig. 18. Pressure series for 4 different elevations on the plate in a compressible air-pocket impact.

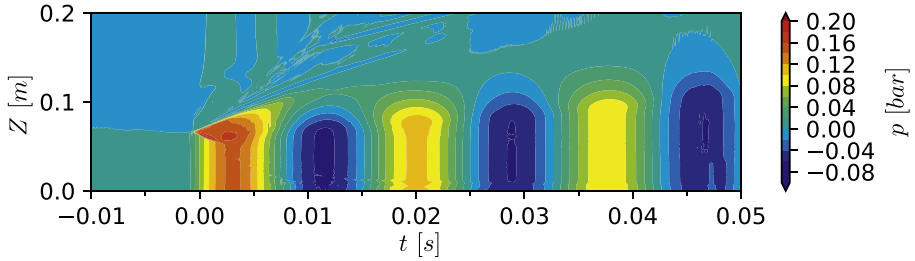

Fig. 19. Spatio-temporal representation of the wall pressure in the compressible air-pocket impact.

4.3. Flip-through or low-areated impact

Now the flip-through or low-areated impact is evaluated. This kind of wave breaking impact only occurs in limited configurations, where the amount of air encapsulated between the liquid and the wall is small. It produces higher peak pressures than the air-pocket as well as more violent upwards water jets. Following the same procedure as in the air-pocket impact, a first qualitative analysis is carried out regarding three snapshots during the impact interval (see Fig. 20). The selected instants are: before the impact, the instant where the highest pressure peak is reached and the initialisation of the splash. The complete impact phenomenon occurs over a relative short time interval of 9 *ms*. From Fig. 20a for instants before the impact happens, only the lower part of the wave is in contact with the wall. It is already exerting a momentum pushing the fluid upwards to avoid the obstacle, similarly as what has been referred as the slightly breaking case in Bullock et al. (2007). Above this point, a relatively large water front is nearly parallel to the wall. The air is flowing out fast from the small cavity. In this computation, the upward velocity will not be fast enough to liberate all the air before the incoming wave front meets the wall resulting in a very small fraction of air entrapment (see Fig. 20b). At this moment the superposition of the fast deceleration of the wave front and the upward jet avoiding the obstacle lead to a highly localised pressure. Similarly as in the air-pocket situation, a compression and expansion process happens now with much higher frequencies due to the smaller size of air cavity. Finally, all the momentum is transferred upwards creating a violent vertical water jet.

This wave breaking impact type is regarded as the limit between the slightly breaking phenomenon and the air-pocket impact, it is then highly sensitive to the wave parameters. Fig. 21 depicts numerical-experimental comparisons, first in terms of free-surface profile before impact and second in terms of pressure distribution at different locations on the plate. The experimental parameters employed were: a wave amplitude of 0.0627 *m* and a water depth of 0.7185 *m* for the water depth before the sloped beach. Here, the numerical solitary wave generation inputs are a wave amplitude of 0.076 *m* and a water depth of 0.7185 *m* to achieve the profile presented in Fig. 21a. A similar impact point elevation is achieved in both cases, however, two major differences are presented in terms of higher air entrapment during the experiments and a lower experimental wave height, both of which could be attributed to the different wave maker types. In Fig. 21b, the pressure distribution is presented at the maximum pressure instant. The pressurised area starts both in experiments and numerics at $Z = 0.07$ *m* with a steep gradient towards the maximal pressure. The experimental pressure sensor at 0.063 *m* recorded the peak pressure in two transverse sections (see Fig. 8b of Sect. 3). This situation is also reproduced on the simulation where a similar magnitude of this peak is reproduced and at a slightly lower elevation of $Z = 0.06$ *m*. Next, the pressure gradient has

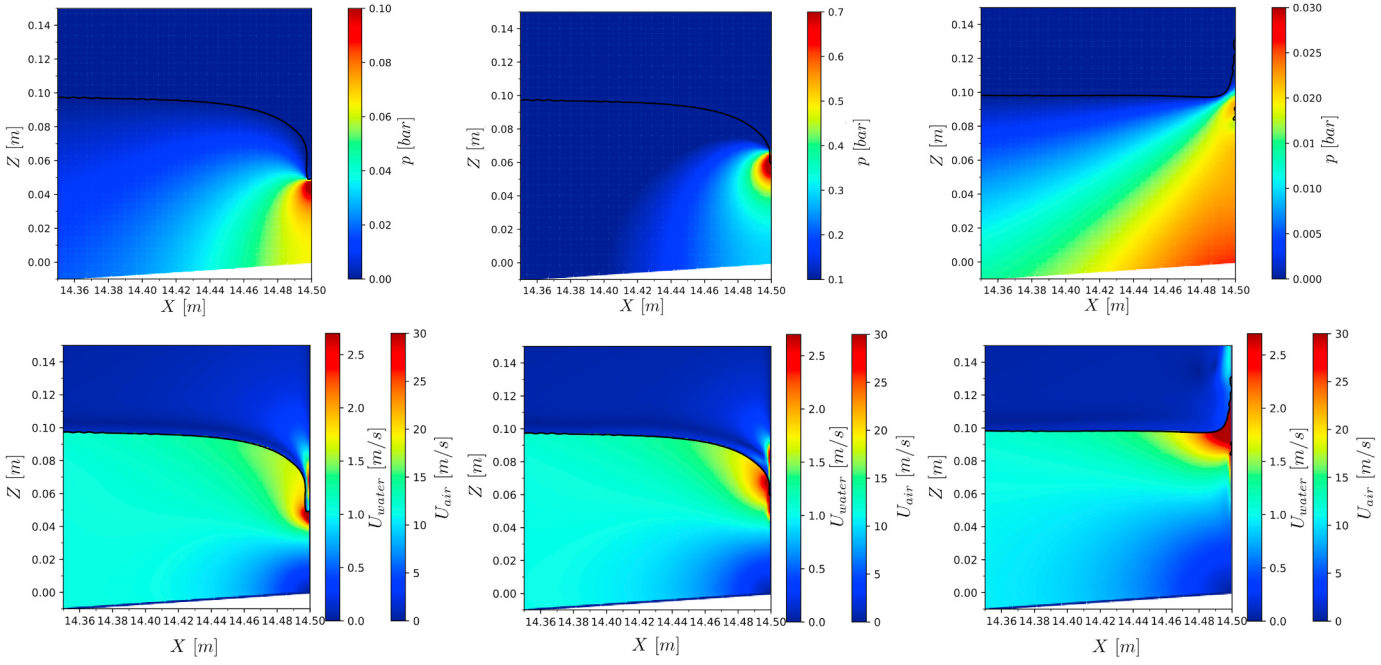

(a) Before the impact $t = -0.001$ *s* (b) Impact instant $t = 0$ *s* (c) Splash after the impact $t = 0.008$ *s*

Fig. 20. Two phase flip-through impact under the compressibility assumption using $dh = 0.5$ *mm*. Solid line corresponds to the interface. Top: pressure evolution during the impact * Notice the change in the colormap range. Bottom: velocity magnitude for air and water.

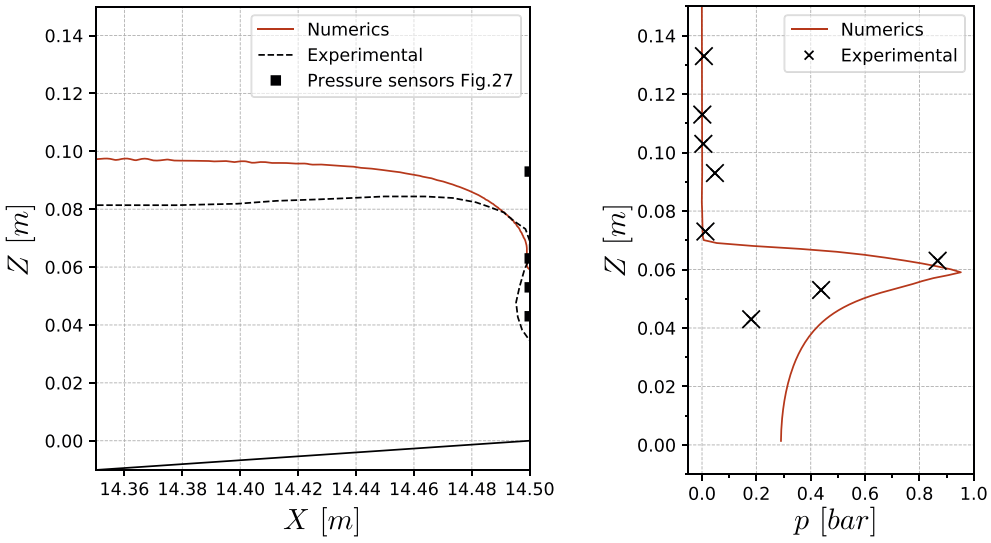

(a) Free surface

(b) Pressure distribution on the wall at $t = 0\,s$

Fig. 21. Free surface comparison at the impact moment. Numeric values of $\alpha = 0.5$.

higher values in the experiments regarding the sensors inside the air cavity. This is attributed to the cushioning effect of a higher fraction of air.

Three relevant pressure series, referred to as black squares on Fig. 21a, are studied on Fig. 22. Let us start from the highest location $Z = 0.093\,m$ above the impact point. Experimentally, an initial noisy behaviour is attributed to the high speed air flowing out from the cavity producing momentaneous subatmospheric values. These are also captured on the simulation, though, in lower magnitudes of $-0.005\,bar$ compared to the experimental minimum of $-0.03\,bar$. After approximately $4\,ms$, there is an experimental pressure rise which is well captured by the simulation on an initial stage. Numerically, at $t = 0.01\,s$ the simulation reaches a maximum of $0.03\,bar$ and starts a plateau of $0.01\,bar$ that last for $0.3\,s$. This pressure rise has two main origins: an initial rise produced by the water jet velocities of $1 - 2\,m/s$ and a second, by the hydrostatic pressure as the water ascends the wall. After the initial pressure rise the experiments rebound to higher values of $0.08\,bar$. The main reason for this discrepancy is due to a thermal shock produced by the difference of temperature between the sensor and the water during wetting process.

Next, the impact point is evaluated at $Z = 0.063\,m$ during the experiments and at $Z = 0.06\,m$ on the simulation. The top left part of Fig. 22 presents a detail of the impact interval. At the location where the water front strikes the wall, the pressure rockets to $0.9\,bar$ in less than

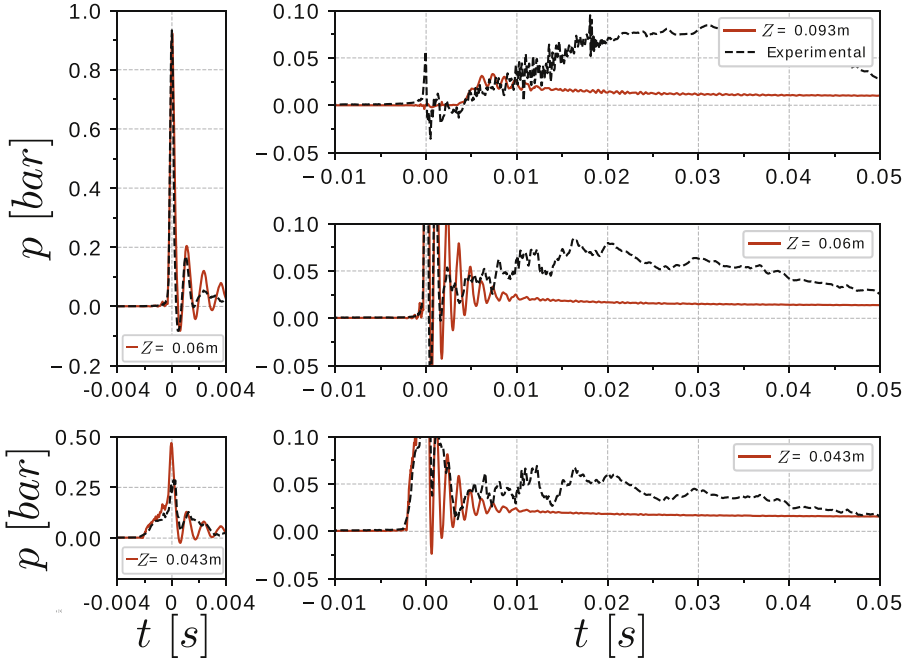

Fig. 22. Pressure series for 3 different elevations on the plate in a compressible flip-through impact.

0.3 *ms*. This is accurately captured by the numerical simulation. Although, after the impact a sudden pressure drop to a minimum of -0.08 *bar* is followed by an oscillatory behaviour linked to the compression and expansion of the cavity. Here, the obtained frequency with $f \simeq 1000$ *Hz* is much higher than with the air pocket configuration due to lower volume of the cavity. These oscillations are accurately captured numerically until the second expansion where the experiments present a faster damping, probably due to 3D effects. After the impact, the simulation presents a stable dynamic pressure as it happens in higher elevations on the plate. On the contrary, in the experiments, a higher value of pressure is recorded most probably coming from the aforementioned thermal shock on the pressure sensor.

The region below the impact point ($Z = 0.043\ m$) is already wet and receiving gradually pressure by the incoming liquid before the impact occurs. Approximately 2 *ms* before the water front strikes the wall, the pressure starts rising gradually. This happens as the water changes the velocity direction from being perpendicular to parallel to the wall together with a deceleration. The sensor is located on the water region during the simulation while, presumably, it is inside the air cavity in the experiments. Regarding the pictures extracted from the experiments an unclear interface is defined in this stage as the cavity is a mixture of air bubbles and water. This explains a lower peak pressure of 0.28 *bar* in this area attenuated by the air on the experiments while a peak of 0.46 *bar* is numerically captured with pure liquid. The compression and expansion of the air entrapped is absorbed around the impact point. Here the first expansion reaches numerically a subatmospheric pressure of -0.015 *bar* while in the experiments falls to a positive value of 0.06 *bar*. Again the damping is underestimated under the 2D configuration as well as the splash phenomenon which is reaching lower maximal value while getting closer to the channel bottom. However, a fairly good agreement between the experimental and numerical pressure record is presented on these graphs of Fig. 22 which gives confidence in the numerical assumptions and the computations run.

Finally, a spatio-temporal representation of the pressure field over the plate is presented on Fig. 23. Before the impact ($t \leq 0\ s$), the lower parts of the plate are being slightly and gradually pressurised as the wave arrives. At the impact moment, a very intense peak pressure is localised around the impingement point. And generally speaking, the whole area beneath this point will reach values of ≈ 0.3 *bar*, that are higher than in the air-pocket configuration. In contrast, these high loads will only last a short period of time. And then, high frequency compression-expansion oscillations start.

5. 3D incompressible solitary wave impact onto a vertical wall

In this section a three dimension geometry is employed to model the air-pocket impact. The motivation of this approach is to measure the influence of the air outflow from the cavity. The experimental setup allowed this phenomenon by keeping a backlash between the impact plate and the lateral walls (see Kimmoun et al., 2009). This is expected to have a direct influence on the pressure oscillations inside the air-cavity presented in Sec. 4.2. This simulation aims to reproduce the short interval of time when the impact occurs while keeping the refined spatial and temporal discretisations. For this purpose, the general idea is to reproduce only the impact region for the impact duration, and not the whole propagation stage which would have been time consuming in 3D. In other words, the assumption is made that, during the impact process, most of the channel length is not affected by this phenomenon and vice versa.

The presented simulation is an extrusion on the Y direction of the final meters of the 2D wave channel during the overturning process. To do so, an OpenFOAM existing tool called *mapFields* has been used. The cell centre fields from the source mesh are interpolated by proximity to the target mesh cell centre at the indicated time. This time is chosen so that the less time steps have to be computed on the 3D mesh before the impact occurs together with that the incoming wave should not already be affecting the wall in terms of pressure. The employed 3D geometry is presented in Fig. 24a. The last 30 *cm* of the 2D channel are extruded on the Y direction. Behind the impact plate 10 *cm* are added on the X direction which are connected to the main channel through the a 2 *mm* width backlash as in the experiments. Regarding the mesh, two differentiated regions on the vertical direction are defined. The lower, beneath the dashed grey line (Fig. 24a), will keep an aspect ratio of 1 between X and Z (cell length being $dh = 1\ mm$). Above this, which will remain out from the water and the interface region until the run-up, a geometrical gradation is employed on the vertical direction. On the Y direction, four equidistant cells of $dh_y = 0.5\ mm$ are employed to model the backlash width. A geometrical gradation of the plate region on the Y direction is employed where the central cells are double size, then $dh_Y = 1\ mm$, compared to the near wall cells. Back of the plate, the gradation on the Y direction starts from $dh_y = 0.5\ mm$ to 1 *mm*. With these assumptions, and using a channel width of $B = 0.15\ m$, the mesh had 4.9 millions cells. The simulation of the $0.2\ s$ impact process using a maximum Courant number of 0.5 approximately takes 41 h with 28 cores of an Intel Broadwell (2.4 GHz) at the CRIANN. Here, the computation is highly constrained by the Courant condition around the backlash when the fast outflow of air from the cavity drastically drops the time-step short before the impact and hence increases the computational time.

The employed boundary conditions are set such as: solid walls with a no slip condition for the lateral wall close to the backlash and the bottom. The impact plate and the end of the channel boundary are also defined as solid walls with a no slip condition. However, aiming to reduce the computational costs of the simulation by only modelling a half of the wave channel on the Y direction, a symmetric boundary condition is set on the central plane. The real half of the channel width is in fact $B_{exp} = 0.32\ m$ but this will not have a major impact on the obtained results. The top plane is defined as an open boundary with a total pressure condition. Finally, the most critical boundary is the inlet plane where a similar inflow velocity as in the 2D configuration section is imposed. Here, a constant value of velocity on the horizontal direction is set on each wet cell. More precisely, a constant velocity of $U = 1.1\ m/s$ is imposed on the inlet based on an extraction from the 2D configuration section 14.2 *m* away from the wave maker. All the other variables such as the pressure, the liquid volume fraction are extracted from the air-pocket configuration presented in Sec.4.2 at $t = 8.33\ s$.

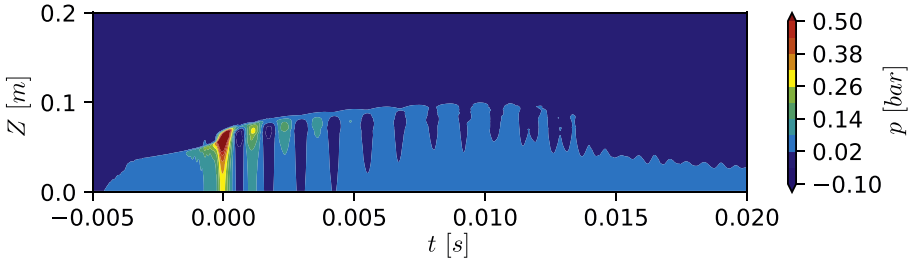

Fig. 23. Spatio-temporal representation of the wall pressure in the compressible flip-through impact.

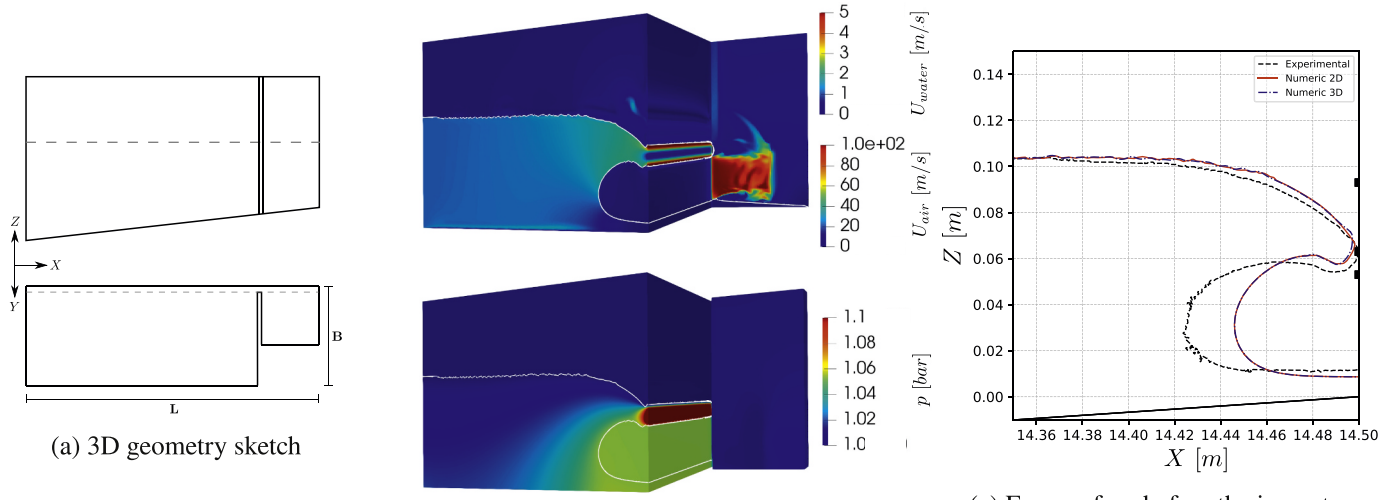

(a) 3D geometry sketch

(b) 3D velocity and pressure fields after the impact

(c) Free surface before the impact

Fig. 24. 3D simulation overview.

Fig. 24b presents the 3D velocity and pressure fields. Regarding the velocity fields, the water spike decelerates fast when meeting the wall and splits into two high speed jets with velocities up to $5m/\,s$. The air phase reaches high-speed velocities as it escapes from the entrapped cavity through the aforementioned back-lash, as presented on the back of the image. The pressure fields on the water region have a similar representation as in the 2D compressible configuration. However, the air cavity is depressurised gradually as the air escapes. Here, the pressure gradient is very strong and spatially localised close to the back-lash at these initial moments. After running 25 *ms*, the free surface extracted from a central transverse section is represented and compared on Fig. 24c. The 2D and the 3D simulations are almost superposed with slightly lower curvatures of the water spike on the 3D computation due to coarser spatial discretisation on the X and Y direction. The experimental free surface is also represented and the major differences lie in the larger air cavity and a slightly wider water spike experimentally.

Now three representative pressure series, represented by the black squares on Fig. 24c, are analysed on Fig. 25. A pressure sensor located above the impact point, $Z = 0.093\,m$, will capture principally the splash phenomenon with dynamic pressure range values. Here the pressure rise occur at similar instants for both experiments and numerics, approximately 5 *ms* after the peak pressure. The pressure rise have similar slopes reaching 0.06 *bar* numerically and higher values of ≈ 0.1 *bar* experimentally, which will correspond to velocities between $2.5-3\,m/s$. After, the loss of pressure is much faster numerically stabilising around 0.018 *bar* during the run-up phase.

In the impact region, at $Z = 0.063\,m$, two different phenomena

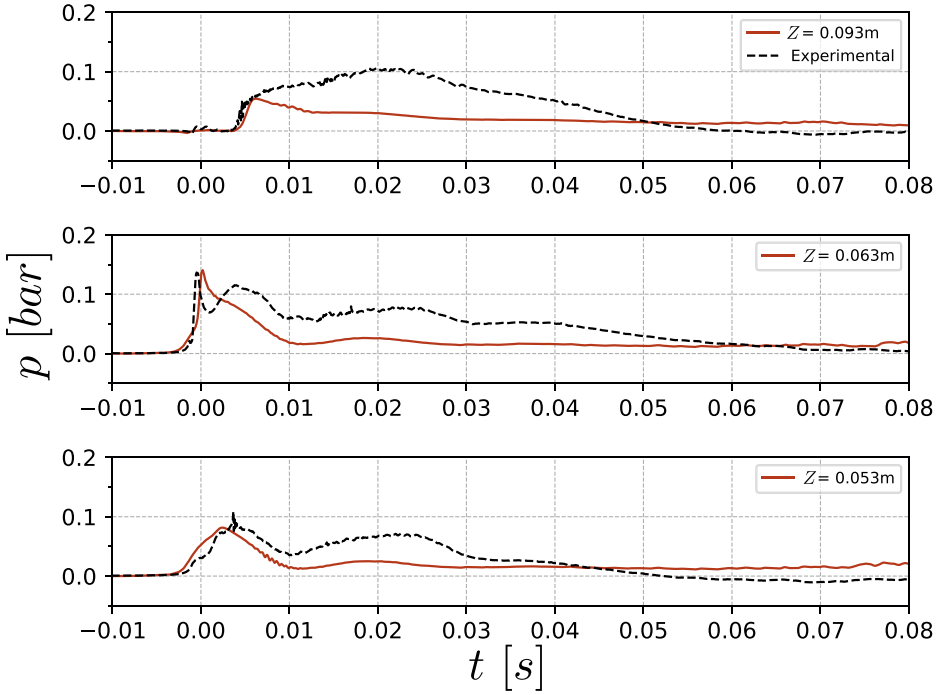

Fig. 25. Pressure series for 3 different elevations on the plate in a compressible air-pocket impact 3D configuration.

explain the recorded pressure series, either experimentally or numerically. The first explanation is related to the cavity compression and overlaps with the temporal serie inside the air cavity region ($Z = 0.053\,m$). The second one with higher temporal derivative is related to the impulsive event, the impact of the water spike. A peak pressure of $0.14\,bar$ is numerically obtained and accurately compared to the experiments, although slightly shifted in time. This delay is related to the fact that the maximum pressure peak experimentally of $0.18\,bar$ is reached in a gauge located at $Z = 0.073\,m$ slightly after the peak pressure at $Z = 0.063\,m$. Numerically the impact region has a slightly lower elevation and the maximum pressure value is reached at $Z = 0.063\,m$, as it happened in the 2D configuration (see Fig. 18).

After the impact a second rebound is presented experimentally with values up to $0.12\,bar$ simultaneously with the maximal compression of the air cavity. This second rebound is achieved numerically with lower values of approximately $\approx 0.1\,bar$. However, the time span between the peak and the rebound is much shorter numerically as the cavity compression is happening earlier. After this rebound, the air flows out from the cavity through the backlash as it gets compressed and a pressure drop occurs without reaching subatmospheric values. Next, a slightly pressure rebound occurs ($0.01\,s < t < 0.03$) as the water splash blocks partially the backlash decelerating the air outflow and, thus, compressing the air cavity again. Here the numeric pressure of $0.03\,bar$ largely underestimate the experimental $0.09\,bar$, which may be due to a lower blockage of the backlash. Finally, inside the air cavity at $Z = 0.053\,m$, a first pressure rebound is well captured numerically in terms of magnitude at $0.08\,bar$ together with a $2\,ms$ time shift. An experimental peak pressure occurs followed by fast oscillation when the cavity reaches it maximal compression ($t \approx 0.005\,s$), which should be further studied. After, the pressure falls experimentally and numerically. Although, as it has just been mentioned, the second pressure rebound is being underestimated numerically due to the thermal shock effect on the experimental pressure sensor.

Fig. 26 present the Spatio-temporal representation of the pressure history on the impact plate. Initially a similar behaviour occurs as in the 2D configuration (see Fig. 19), while the air cavity is being compressed before the impingement. Just after the water spikes meets the wall, a localised pressure rise up to $0.14\,bar$ is generated slightly below the impact point. As the splash phenomenon develops, it pressurises the wet area. At the same time, the cavity is being compressed until a maximum value is reached pushing the air to outflow through the backlash. The pressure oscillations observed on the 2D configuration are not observable anymore, which was expected in this 3D configuration.

6. Conclusion

This paper presents a numerical investigation of the fluid impact loads on a solid body with special emphasis on convergence of the computations and evaluation of the accuracy of the obtained pressure records. Although in real life condition, a wave train is continuously impinging a breakwater, the choice of a single solitary wave was made to enable a better numerical-experimental comparison on this single event. The used numerical tool is the Finite Volume software suite OpenFOAM, for which different numerical assumptions were made: an incompressible or a compressible formulation of the solver. And the comparisons and validations were regularly made on either the pressure time series or the pressure impulse.

To start with, an idealised wave impact test-case was employed to validate the pressure impulse convergence of the present model under the incompressible assumption. An analytical value of the pressure impulse exists for this idealised test case first introduced by Cooker and Peregrine (1990). Under this incompressible assumption, a remarkable good convergence of the pressure impulse towards the analytic solution proposed by Cooker et al. was demonstrated by the solver during a spatial and a temporal convergence study. However, the maximum recorded pressure kept increasing when the mesh and time steps were refined. Similar tests were run on a 2D air-pocket impact configuration experimentally documented in the literature by Kimmoun et al. (2009). Again, a good convergence of the pressure impulse is obtained but the maximum pressure peak never converged and kept increasing with the mesh refinement. Additionally, the treatment of the air cavity in such an air-pocket impact lead to some numerical complexity under such an incompressible assumption. To conclude on the use of this incompressible assumption, one can say that the simulations converged. But the pressure records are not a good measure to evaluate the convergence. Furthermore, in such impulsive events, the numerically obtained pressure records could give completely erroneous loads which may be very problematic when designing a breakwater. To the authors point of view, the incompressible assumption should be avoided when accurate pressure measurements are expected. To be more precise, our work aroused the necessity of a compressible model when one of these two conditions comes: the air is playing a role and/or the impact has an impulsive behaviour. This is clearly the case for air-pocket and flip-through impacts.

Secondly, the compressible assumption was tested. Making use of the idealised case, a good convergence of the pressure peak was achieved and validated with respect to the acoustic pressure theory. Then, testing the air-pocket impact in a 2D configuration showed converged results in terms of peak pressure using the compressible OpenFOAM solver. The solitary wave was used to reproduce the breaking impact conditions and compared with the experimental records of Kimmoun et al. (2009) in terms of surface elevation, velocity and recorded wall pressure. The difference of the wave-maker between a flap type (experiments) and a piston type (numerics) produced some minor discrepancies on the free surface profile before the impact. But the computations of both 2D high-areated (air-pocket) or low-aerated (flip-through) wave breaking cases proved satisfactory results in terms of impact peak pressure magnitude compared with the experiments. They also proved the ability to capture the air compressibility effects, principally on the low-aerated impact. For the air-pocket configuration, the air cavity behaviour has shown to be highly dependant on the escape possibility for air. Of course, the pure 2D configuration of the present work lead to a compression-expansion of the cavity facing the impossibility of the air to escape and, thus, producing a pressure oscillatory behaviour with subatmospheric values. These pure 2D configurations are most probably never encountered in real life and a 3D configuration gave more

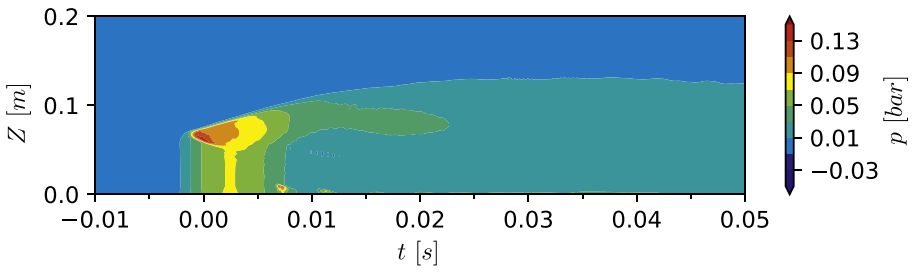

Fig. 26. Spatio-temporal representation of the wall pressure in the 3D air-pocket impact configuration.

accurate results when compared to the experimental pressure records. In fact, in the experiments, the air was able to flow through two backlashes short before and also during the impact instant.

However, for both the 2D and 3D configurations, a numerical underestimation of the quasi-hydrostatic pressure just after the impact is presented and related to the occurrence of a thermal shock produced by the difference of temperature between the experimental sensor and the water. Nevertheless, numerical and experimental pressure records tends to give very similar pressure time series for the different tested configurations. Owing to the physics of wave impact, the pressure records showed a high degree of spatial and temporal scattering; and the highest pressure recorded was by far on the low-aerated impact. And, under the compressible assumption, most of these complex phenomena were accurately reproduced numerically. For real life configuration, a full 3D well resolved compressible model would inevitably give the best results but this study also showed the associated computational costs. For real design phase of coastal structure, a 3D well resolved model will probably not be feasible and 2D compressible approach may reveal sufficient in most cases.

In summary, the tool box OpenFOAM demonstrated to be suitable for assessing fluid impulsive loads on structures and extended to wave loads for coastal and ocean engineering applications. An acceptable convergence of the results in terms of maximum pressure gives confidence for future design work. Great variability of maximum loads have been identified and the air entrapment has demonstrated to be a key parameter, as it has been reported before, both experimentally and numerically.

7. CRediT authorship contribution statement

Marc Batlle Martin: Software, Validation, Formal analysis, Investigation, Writing - Original Draft. **Grégory Pinon:** Conceptualization, Validation, Formal analysis, Investigation, Resources, Writing - Review & Editing, Supervision, Funding acquisition. **Julien Reveillon:** Formal analysis, Investigation, Writing - Review & Editing, Supervision, Funding acquisition. **Olivier Kimmoun:** Formal analysis, Investigation, Resources, Writing - Review & Editing.

Declaration of competing interest

The authors declare that they have no known competing financial interests or personal relationships that could have appeared to influence the work reported in this paper.

Acknowledgements

M. Batlle Martin acknowledges the financial support for his PhD grant from the regional council of Normandie. The authors acknowledge the financial support of the CPER-ERDF program DIADEMAR funded by the Normandy Regional Council and the European Union. The present work was performed on computing resources provided by CRIANN (Normandy, France). The authors acknowledge the financial support of the Agence Nationale de la Recherche, through the program Investissements d'avenir - LabEx EMC3 via the project PERCUSS.

References

Bagnold, R.A., 1939. Interim report on wave-pressure research. (includes plates and photographs). J. Inst. Civil Eng. 12, 202–226. https://doi.org/10.1680/ijoti.1939.14539. URL: https://doi.org/10.1680/ijoti.1939.14539. arXiv: https://doi.org/10.1680/ijoti.1939.14539.

Braeunig, J.P., Brosset, L., Dias, F., Ghidaglia, J.M., 2009. Phenomenological study of liquid impacts through 2d compressible two-fluid numerical simulations. In: Proceedings of the Nineteenth (2009) International Offshore and Polar Engineering Conference. The International Society of Offshore and Polar Engineers (ISOPE), Osaka, Japan, pp. 21–29 iSBN : 978-1-880653-53-1 Lien vers le texte intégral. https://hal.archives-ouvertes.fr/hal-00605428. http://www.isope.org/publications/proceedings/ISOPE/ISOPE/2009/start.htm.

Bullock, G., Obhrai, C., Peregrine, D., Bredmose, H., 2007. Violent breaking wave impacts. part 1: results from large-scale regular wave tests on vertical and sloping walls. Coast Eng. 54, 602–617. https://doi.org/10.1016/j.coastaleng.2006.12.002. http://www.sciencedirect.com/science/article/pii/S037838390600192X.

Cole, R.H., 1948. Underwater Explosions. Princeton Univ. Press, Princeton.

Cooker, M., Peregrine, D., 1990. A model for breaking wave impact pressures. Coastal Engineering Proceedings 1.

Cooker, M.J., Peregrine, D.H., 1995. Pressure-impulse theory for liquid impact problems. J. Fluid Mech. 297, 193–214. https://doi.org/10.1017/S0022112095003053.

Cuomo, G., Allsop, W., Bruce, T., Pearson, J., 2010. Breaking wave loads at vertical seawalls and breakwaters. Coastal Engineering - COAST ENG 57, 424–439. https://doi.org/10.1016/j.coastaleng.2009.11.005.

Damián, S.M., 2013. An Extended Mixture Model for the Simultaneous Treatment of Short and Long Scale Interfaces. Ph.D. thesis.. https://doi.org/10.13140/RG.2.1.3182.8320.

Deshpande, S.S., Anumolu, L., Trujillo, M.F., 2012. Evaluating the performance of the two-phase flow solver interFoam. Comput. Sci. Discov. 5, 014016 https://doi.org/10.1088/1749-4699/5/1/014016.

Francois, M.M., Cummins, S.J., Dendy, E.D., Kothe, D.B., Sicilian, J.M., Williams, M.W., 2006. A balanced-force algorithm for continuous and sharp interfacial surface tension models within a volume tracking framework. J. Comput. Phys. 213, 141–173. https://doi.org/10.1016/j.jcp.2005.08.004. http://www.sciencedirect.com/science/article/pii/S0021999105003748.

Goda, Y., 2010. Random Seas and Design of Maritime Structures, third ed. WORLD SCIENTIFIC. https://doi.org/10.1142/7425 https://www.worldscientific.com/doi/abs/10.1142/7425. arXiv: https://www.worldscientific.com/doi/pdf/10.1142/7425.

Guilcher, P., Oger, G., Brosset, L., Jacquin, E., Grenier, N., Le Touzé, D., 2010. Simulation of liquid impacts with a two-phase parallel SPH model. In: Proceedings of 20th International Offshore and Polar Engineering Conference. June 20-26, Bejing, China.

Hattori, M., Arami, A., Yui, T., 1994. Wave impact pressure on vertical walls under breaking waves of various types. Coast Eng. 22, 79–114. https://doi.org/10.1016/0378-3839(94)90049-3. special Issue Vertical Breakwaters. http://www.sciencedirect.com/science/article/pii/0378383994900493.

Higuera, P., Lara, J.L., Losada, I.J., 2013. Realistic wave generation and active wave absorption for Navier–Stokes models: application to openfoam®. Coast Eng. 71, 102–118. https://doi.org/10.1016/j.coastaleng.2012.07.002. http://www.sciencedirect.com/science/article/pii/S0378383912001354.

Higuera, P., Liu, P.L.F., Lin, C., Wong, W.Y., Kao, M.J., 2018. Laboratory-scale swash flows generated by a non-breaking solitary wave on a steep slope. J. Fluid Mech. 847, 186–227. https://doi.org/10.1017/jfm.2018.321.

Hofland, B., Kaminski, M., Wolters, G., 2011. Large scale wave impacts on a vertical wall. Coastal Engineering Proceedings 1 structures–15.

Hu, Z.Z., Mai, T., Greaves, D., Raby, A., 2017. Investigations of offshore breaking wave impacts on a large offshore structure. J. Fluid Struct. 75, 99–116. https://doi.org/10.1016/j.jfluidstructs.2017.08.005. http://www.sciencedirect.com/science/article/pii/S0889974616301451.

Hysing, S., 2006. A new implicit surface tension implementation for interfacial flows. Int. J. Numer. Methods Fluid. 51, 659–672. https://doi.org/10.1002/fld.1147. https://onlinelibrary.wiley.com/doi/abs/10.1002/fld.1147. arXiv: https://onlinelibrary.wiley.com/doi/pdf/10.1002/fld.1147.

Issa, R.I., 1986. Solution of the implicitly discretised fluid flow equations by operator-splitting. J. Comput. Phys. 62, 40–65. https://doi.org/10.1016/0021-9991(86)90099-9.

Jensen, A., 2018. Solitary wave impact on a vertical wall. Eur. J. Mech. B Fluid 73. https://doi.org/10.1016/j.euromechflu.2018.05.004.

Kimmoun, O., Ratouis, A., Brosset, L., 2010. Sloshing and scaling: experimental study in a wave canal at two different scales. In: Proceedings of 20th International Offshore and Polar Engineering Conference, June, pp. 20–26.

Kimmoun, O., Scolan, Y., Malenica, S., 2009. Fluid structure interactions occurring at a flexible vertical wall impacted by a breaking wave. In: The Nineteenth International Offshore and Polar Engineering Conference. International Society of Offshore and Polar Engineers.

Lagrange, J.L., 1811. Mécanique Analytique. 1.

Larsen, B.E., Fuhrman, D.R., Roenby, J., 2018. Performance of Interfoam on the Simulation of Progressive Waves arXiv:1804.01158.

Lind, S., Stansby, P., Rogers, B., Lloyd, P., 2015. Numerical predictions of water–air wave slam using incompressible–compressible smoothed particle hydrodynamics. Appl. Ocean Res. 49, 57–71. https://doi.org/10.1016/j.apor.2014.11.001. URL: http://www.sciencedirect.com/science/article/pii/S0141118714001126.

Liu, S., Gatin, I., Obhrai, C., Ong, M.C., Jasak, H., 2019. Cfd simulations of violent breaking wave impacts on a vertical wall using a two-phase compressible solver. Coast Eng. 154, 103564. https://doi.org/10.1016/j.coastaleng.2019.103564. URL: http://www.sciencedirect.com/science/article/pii/S0378383919301620.

Lugni, C., Brocchini, M., Faltinsen, O.M., 2010a. Evolution of the air cavity during a depressurized wave impact. ii. the dynamic field. Phys. Fluids 22, 056102. https://doi.org/10.1063/1.3409491.

Lugni, C., Miozzi, M., Brocchini, M., Faltinsen, O., 2010b. Evolution of the air-cavity during a depressurized wave impact. part i: the kinematic flow field[j]. Physics of Fluids - PHYS FLUIDS 22. https://doi.org/10.1063/1.3407664.

Mai, T., Hu, Z., Greaves, D., Raby, A., 2015. Investigation of Hydroelasticity: Wave Impact on a Truncated Vertical Wall.

Marrone, S., Colagrossi, A., Di Mascio, A., Le Touzé, D., 2015. Prediction of energy losses in water impacts using incompressible and weakly compressible models. J. Fluid Struct. 54, 802–822. https://doi.org/10.1016/j.jfluidstructs.2015.01.014. http://www.sciencedirect.com/science/article/pii/S0889974615000195.

Marrone, S., Colagrossi, A., Di Mascio, A., Le Touzé, D., 2016. Analysis of free-surface flows through energy considerations: single-phase versus two-phase modeling. Phys. Rev. 93 https://doi.org/10.1103/PhysRevE.93.053113.
Oger, G., Guilcher, P., Jacquin, E., Brosset, L., Deuff, J., Le Touzé, D., et al., 2010. Simulations of hydro-elastic impacts using a parallel SPH model. Int. J. Offshore Polar Eng. 20, 181–189.
Oumeraci, H., Klammer, P., Partenscky, H., 1993. Classification of breaking wave loads on vertical structures. J. Waterw. Port, Coast. Ocean Eng. 119, 381–397.
Patankar, S.V., Spalding, D.B., 1972. A Calculation Procedure for Heat, Mass and Momentum Transfer in Three-Dimensional Parabolic Flows.
Roenby, J., Bredmose, H., Jasak, H., 2016. A computational method for sharp interface advection. Open Science 3, 160405.
de Rouville, A., Besson, P., Petry, P., 1938. État actuel des études internationales sur les efforts dus aux lames.
Schlichting, H., Gersten, K., 1979. Boundary-layer Theory.
Stevenson, T., 2011. The Design and Construction of Harbours: A Treatise on Maritime Engineering. Cambridge Library Collection - Technology, Cambridge University Press. https://doi.org/10.1017/CBO9780511997020.
Sumer, B., Jensen, P., Sørensen, L., Fredsøe, J., Liu, P., Carstensen, S., 2010. Coherent structures in wave boundary layers. part 2. solitary motion. J. Fluid Mech. 646, 207–231. https://doi.org/10.1017/S0022112009992837.
Vukčević, V., Jasak, H., Malenica, Š., 2016. Decomposition model for naval hydrodynamic applications, part i: computational method. Ocean. Eng. 121, 37–46. https://doi.org/10.1016/j.oceaneng.2016.05.022. http://www.sciencedirect.com/science/article/pii/S0029801816301342.
Wemmenhove, R., Luppes, R., Veldman, A.E., Bunnik, T., 2015. Numerical simulation of hydrodynamic wave loading by a compressible two-phase flow method. Comput. Fluid 114, 218–231. https://doi.org/10.1016/j.compfluid.2015.03.007. http://www.sciencedirect.com/science/article/pii/S0045793015000808.

Marc Batlle Martin has been a PhD student for the past 2 years at Laboratoire Ondes et Milieux Complexes, Le Havre. He studied a MEng Civil in the Polytechnic University of Madrid. He is interested on computational fluid dynamics and their application on offshore, coastal and hydraulic engineering. He has participated as a speaker in multiple conferences: “VII International Conference on Computational Methods in Marine Engineering”, “16èmes Journées de l’Hydrodynamique” and “4th French/Belgian OpenFOAM users conference” among others.